

RESEARCH ARTICLE

10.1002/2016JD026421

Key Points:

- Multimodel evaluation of aerosol transport showed some common features amongst the models that were distinct from satellite observations
- The aerosol plume top heights over land are, in general, captured by the models irrespective of different injection height assumptions
- The bulk of the modeled aerosol layers over the ocean occurs at levels 1–2 km lower than the corresponding satellite observations

Correspondence to:

S. Das,
das22@purdue.edu

Citation:

Das, S., H. Harshvardhan, H. Bian, M. Chin, G. Curci, A. P. Protonotariou, T. Mielonen, K. Zhang, H. Wang, and X. Liu (2017), Biomass burning aerosol transport and vertical distribution over the South African-Atlantic region, *J. Geophys. Res. Atmos.*, 122, doi:10.1002/2016JD026421.

Received 22 DEC 2016

Accepted 27 MAY 2017

Accepted article online 31 MAY 2017

Biomass burning aerosol transport and vertical distribution over the South African-Atlantic region

Sampa Das¹ , H. Harshvardhan¹ , Huisheng Bian^{2,3} , Mian Chin³ , Gabriele Curci^{4,5} , Anna P. Protonotariou⁶ , Tero Mielonen⁷ , Kai Zhang⁸ , Hailong Wang⁸ , and Xiaohong Liu⁹ 

¹Department of Earth, Atmospheric and Planetary Sciences, Purdue University, West Lafayette, Indiana, USA, ²Joint Center for Earth Systems Technology, UMBC, Baltimore, Maryland, USA, ³NASA Goddard Space Flight Center, Greenbelt, Maryland, USA, ⁴Department of Physical and Chemical Sciences, University of L'Aquila, L'Aquila, Italy, ⁵Center of Excellence in Telesensing of Environment and Model Prediction of Severe events, University of L'Aquila, L'Aquila, Italy, ⁶Department of Physics, University of Athens, Athens, Greece, ⁷Finnish Meteorological Institute, Kuopio, Finland, ⁸Pacific Northwest National Laboratory, Richland, Washington, USA, ⁹Department of Atmospheric Science, University of Wyoming, Laramie, Wyoming, USA

Abstract Optically thick smoke aerosol plumes originating from biomass burning (BB) in the southwestern African Savanna during the austral spring are transported westward by the free tropospheric winds to primarily overlie vast stretches of stratocumulus cloud decks in the southeast Atlantic. We evaluated the simulations of long-range transport of BB aerosol by the Goddard Earth Observing System (GEOS-5) and four other global aerosol models over the complete South African-Atlantic region using Cloud-Aerosol Lidar with Orthogonal Polarization (CALIOP) observations to find any distinguishing or common model biases. Models, in general, captured the vertical distribution of aerosol over land but exhibited some common features after long-range transport of smoke plumes that were distinct from that of CALIOP. Most importantly, the model-simulated BB aerosol plumes quickly descend to lower levels just off the western coast of the continent, while CALIOP data suggest that smoke plumes continue their horizontal transport at elevated levels above the marine boundary layer. This is crucial because the sign of simulated aerosol semidirect effect can change depending on whether the bulk of the absorbing aerosols is present within or above the cloud levels in a model. The levels to which the aerosol plumes get subsided and the steepness of their descent vary amongst the models and amongst the different subregions of the domain. Investigations into possible causes of differences between GEOS-5 and CALIOP aerosol transport over the ocean revealed a minimal role of aerosol removal process representation in the model as opposed to model dynamics.

1. Introduction

Open biomass burning (BB) is a major source of trace gases and carbonaceous aerosol particles in the atmosphere. Although BB occurs globally, there are particular features associated with different types of vegetation and climate regimes. The smoke aerosol from BB is composed of strongly absorbing black carbon (BC) particles and fine organic carbon (OC) particles, whose proportions vary according to vegetation type, oxygen availability, and combustion phase [Andreae and Merlet, 2001]. BC is the second most important human emission responsible for climate change as it has an estimated global climate forcing potential of $+1.1 \text{ W m}^{-2}$ with 90% uncertainty bounds of $+0.17$ to $+2.1 \text{ W m}^{-2}$, which is second only to carbon dioxide [Bond et al., 2013]. BC amounts are found to be particularly large during efficient flaming fires, common in the savanna and Cerrado grassland of Africa and South America [Hao et al., 1996]. In the southwestern African Savanna (Figure 1), there is seasonal burning in the Austral spring (July–October) contributing to about one third of the global BB emissions [van der Werf et al., 2010]. The optically thick aerosol plumes produced by this burning are primarily transported westward for thousands of kilometers by the free tropospheric winds over the Atlantic region [Edwards et al., 2006]. However, unlike smoke from industrial activity and biofuels that intermingle with clouds in most regions [Mechoso et al., 2013; Ramanathan et al., 2001], smoke layers in the southeast (SE) Atlantic have been observed to mainly overlie vast stretches of marine stratocumulus (Sc) clouds [Adebiji et al., 2015; Costantino and Bréon, 2010; Wilcox, 2010].

During its transport from land to ocean, the dense BB aerosol layer interacts with the underlying clouds and affects the Earth's radiative balance in more ways than one. It exerts a direct radiative forcing on the

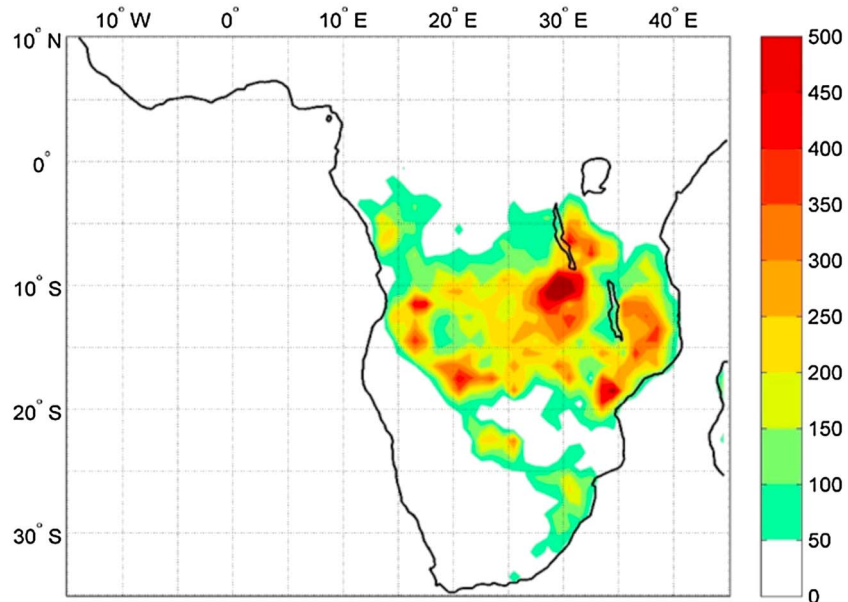


Figure 1. MODIS fire pixel counts (MOD14CM1) are averaged over August and September 2008 to depict the locations of the burning source areas for the peak BB months of the year.

atmosphere, whose sign and magnitude depend upon the optical properties of the aerosol particles as well as on the albedo and coverage of the underlying clouds [Chand *et al.*, 2009; Keil and Haywood, 2003]. An increase in lower free tropospheric buoyancy due to heating of air masses in the absorbing aerosol layer above the clouds and a simultaneous surface cooling resulting from direct radiative effects trap humidity in the boundary layer and cause an increase in cloud cover (fraction) and liquid water path (semidirect effect) [Sakaeda *et al.*, 2011; Wilcox, 2012]. Moreover, as the marine boundary layer (MBL) deepens further offshore and north of 5°S, subsiding aerosol particles become entrained into the MBL and interact with the clouds as cloud condensation nuclei affecting their microphysics (indirect effect) [Costantino and Bréon, 2013; Painemal *et al.*, 2014].

Model-based studies like Sakaeda *et al.* [2011] have found significant estimates of a negative top of the atmosphere semidirect radiative effect (-2.6 W m^{-2}) associated with increased low cloud cover over the oceanic region capable of causing the ocean surface to cool by 1–2 K or more. The changes in the atmospheric heating profile and surface temperature due to the above mentioned aerosol direct and semidirect effects cause a thermally driven anomalous circulation from the western Atlantic toward the west African coast that favors the transport of moisture to the continent from the adjacent ocean. This results in the increase of clouds, water vapor, and eventually precipitation during the wet season [Randles and Ramaswamy, 2010; Roeckner *et al.*, 2006]. Thus, the robust estimation of the aerosol radiative effects by the model simulations is crucial in assessing the effects of aerosol on large-scale circulations and subsequently on regional and global climate. Toward this end, previous model-based studies on absorbing aerosol-cloud interactions [Johnson *et al.*, 2004; Koch and Del Genio, 2010; McFarquhar and Wang, 2006; Penner *et al.*, 2003] and on the direct radiative forcing of carbonaceous aerosol [Abel *et al.*, 2005; Samset *et al.*, 2013] have emphasized that a significant fraction of the uncertainty in the magnitude and sign of the modeled aerosol radiative effects comes from the diversity in the simulated vertical profiles of aerosol concentrations amongst the models. Thus, to be useful for any climate change studies, aerosol simulations must have the ability to reproduce the observed vertical distribution of aerosol (especially with respect to clouds) in addition to their optical thickness and absorbing properties.

Specific to our domain of interest (Figure 2), simulations of aerosol vertical distributions by the Goddard Chemistry Aerosol Radiation Transport (GOCART) model have been evaluated previously using Cloud-Aerosol Lidar with Orthogonal Polarization (CALIOP) observations explicitly [Yu *et al.*, 2010] and also as part of the AeroCom (Aerosol Comparisons between Observations and Models) project [Koffi *et al.*, 2012];

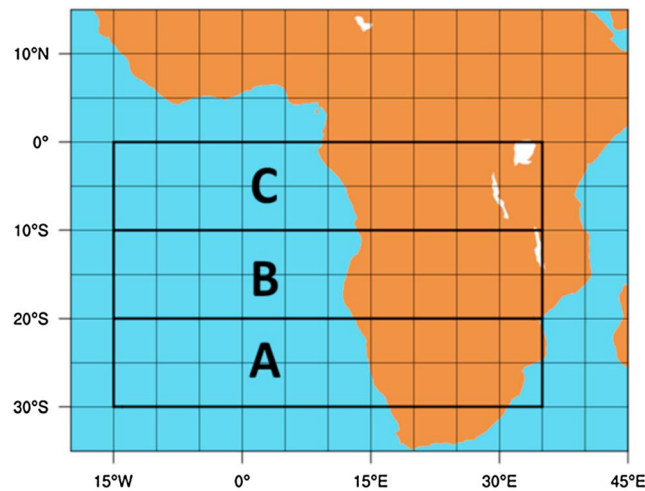


Figure 2. The region of interest is divided into subregions A (30°–20°S, 35°E–15°W), B (20°–10°S, 35°E–15°W), and C (10°S–0°, 35°E–15°W) to distinguish between the different aerosol transport features within the domain.

Koffi et al., 2016]. These studies performed their evaluations only over the South African (SAF) burning source region of our domain but not over the South Atlantic region influenced by long-range transport. *Koffi et al.* [2012] found the shape of the mean aerosol extinction profiles simulated by GOCART and those derived using CALIOP version 3.01 data over SAF (over land) to be in reasonable agreement with each other, but the model underestimated the magnitude of extinctions at different levels within the lowest 4 km above the model surface causing an overall underestimation of model aerosol optical depth (AOD) compared to both MODIS (Moderate Resolution Imaging Spectroradiometer) and CALIOP retrievals.

GOCART was integrated within the Goddard Earth Observing System model (GEOS) as an aerosol module [Colarco *et al.*, 2010] for various applications. More recently, the latest version of GEOS (version 5), coupled to GOCART, was used to produce the Modern-Era Retrospective analysis for Research and Applications Aerosol Reanalysis (MERRAero) global data set [Buchard *et al.*, 2015] that included the assimilation of bias-corrected MODIS-derived aerosol optical depths (AODs) in addition to the assimilation of traditional meteorological parameters (winds, pressure, and temperature fields) [Rienecker *et al.*, 2008]. The assessment of MERRAero BB aerosol properties using independent observational data sets showed that MERRAero AOD estimates were highly correlated with MISR (Multiangle Imaging Spectroradiometer) and AERONET (Aerosol Robotic Network) AOD estimates over our domain. However, MERRAero BB aerosol vertical distribution after long-range transport into the southeast (SE) Atlantic exhibited significant discrepancies compared to CALIOP measurements, as further discussed in section 5.

Extending from the findings of previous studies, the primary objective of our study is to evaluate the simulation of long-range transport and vertical distribution of BB aerosol by GEOS-5-GOCART over the complete South African-Atlantic region using CALIOP observations and compare the simulation with other global aerosol models participating in the recently conducted AeroCom Phase III experiments (described in section 2.2) to find any distinguishing model biases. Since the vertical distribution of BB aerosol in a model depends on a number of physical and chemical processes in addition to the emission source strength, namely, (1) the injection height (vertical distribution of aerosol emissions), (2) the convective transport, (3) dry and wet removal, and (4) physical aging [Allen and Landuyt, 2014], our study also aims to find the most relevant processes in our context, amongst the ones listed, that may be responsible for the discrepancies between the observed and GEOS-5-simulated BB aerosol vertical distribution. The results of this study will help us understand the differences between the models and observations, the possible cause(s) for these differences, and a direction for improvement in model performance in this important region of BB aerosol transport.

The paper is further organized as follows. Section 2 provides a brief description of the GEOS-5-GOCART model configuration and simulations along with an overview of the other AeroCom models used in this study. CALIOP measurements and their quality screening and processing details are explained in section 3. In section 4, we discuss the results from the comparative analysis of model outputs with observations, emphasizing the aerosol vertical distribution and transport from southern Africa to SE Atlantic. This section also discusses CALIOP measurement biases due to the presence of optically thick smoke plumes in the context of our domain. Based on the findings from section 4, possible causes of the differences between GEOS-5 simulations and CALIOP retrievals of aerosol transport over the ocean are investigated in section 5. Finally, the major findings of the study are summarized in section 6.

2. Description of Models

2.1. GEOS-5-GOCART

The GEOS-5 Earth system model is a weather-and-climate-capable model consisting of components for atmospheric circulation and composition, oceanic circulation, land surface processes, and data assimilation [Rienecker *et al.*, 2008]. The model can be operated in different modes, viz., climate mode, data assimilation mode, or replay mode. In the climate mode, the model behaves as a free-running atmospheric general circulation model (AGCM) with prescribed sea surface temperatures, which requires just the initial conditions to make a forecast for a specified time [e.g., Randles *et al.*, 2013]. In assimilation mode, the AGCM is integrated with the Gridpoint Statistical Interpolation atmospheric analysis system that performs a meteorological analysis to adjust the dynamical state (winds, pressure, temperature, and humidity) of the AGCM every 6 h [e.g., Rienecker *et al.*, 2011]. To avoid the computational cost of performing the analysis every time the model is operated, in the replay mode, the model is forced using a previous analysis that was produced using an identical version of the current AGCM [e.g., Bian *et al.*, 2013]. The replay mode is closest to how most offline chemical transport models (CTMs) work. For this study, the model was run in the replay mode using Modern-Era Retrospective Analysis for Research and Applications (MERRA) meteorological analyses to adjust its dynamical state every 6 h. The model was run at 1° (latitude) \times 1.25° (longitude) horizontal resolution with 72 hybrid vertical sigma levels between the surface and 0.01 hPa (about 85 km) to provide 3-hourly outputs of aerosol-related properties.

The aerosol module in GEOS-5 is based on the GOCART model [Chin *et al.*, 2009, 2002]. The module simulates five tropospheric aerosol species: dust, sea salt, black carbon (BC), organic carbon (OC), and sulfate. The aerosol species in GEOS-5 are assumed to be external mixtures that do not interact with each other. The module simulates the following physical processes for aerosols: emission, advection, moist convection, boundary layer turbulent mixing, wet scavenging, and dry deposition [Chin *et al.*, 2002]. The wet scavenging consists of both scavenging in convective updrafts and rainout/washout in large-scale precipitation. Dry deposition includes gravitational settling as a function of aerosol particle size and air viscosity and surface deposition as a function of surface type and meteorological conditions [Chin *et al.*, 2004]. The optical properties of aerosol species are primarily prescribed using the Optical Properties of Aerosols and Clouds data set [Hess *et al.*, 1998].

For this study, we also utilized the carbon monoxide (CO) simulating capability of GOCART, which was incorporated in the GEOS-5 model based on the study of Bian *et al.* [2007]. Simulations of CO using the same BB emission sources as aerosol were important to our study because CO is emitted simultaneously with carbonaceous aerosol during biomass burning but does not undergo the aerosol loss processes of dry and wet deposition [Bian *et al.*, 2010]. This makes CO a good tracer to evaluate the transport processes in the model. The details of how each of the aerosol species are treated in the GOCART module are discussed in Colarco *et al.* [2010], while CO chemistry and transport are discussed in Bian *et al.* [2010]. Here we will only summarize the BB emission sources and chemistry representation of carbonaceous aerosol and CO within the GOCART module.

BC is emitted as 80% hydrophobic and 20% hydrophilic, while OC is 50% hydrophobic and 50% hydrophilic [Chin *et al.*, 2002; Cooke *et al.*, 1999]. The aging process converts the hydrophobic part of the carbonaceous aerosols into hydrophilic phase with an *e*-folding time of 1.1 to 2.5 days [Chin *et al.*, 2002; Maria *et al.*, 2004]. The loss processes for these aerosols involve dry deposition for both hydrophobic and hydrophilic components and wet scavenging for only the hydrophilic aerosols. The chemical processes of loss and generation of CO are accounted by two chemical reactions in the module. CO is dissipated via reaction with the hydroxyl radicals (OH), while it is produced via oxidation of methane (CH₄). However, the generation of CO from the oxidation of nonmethane hydrocarbons is parameterized as a direct emission [Bian *et al.*, 2007]. Both OH and CH₄ concentration fields are derived using the results from a global chemistry and transport model simulation, the Global Modeling Initiative [Bian *et al.*, 2013].

Two sets of simulations were made with the same model configuration but different emission inventories to account for BB emissions of CO and aerosol: the Quick Fire Emission Dataset version 2.4 (QFED2) [Darmenov and da Silva, 2015] and the Global Fire Emission Database version 3.1 (GFED3) [Randerson *et al.*, 2013; van der Werf *et al.*, 2006]. The main difference between the two emission inventories is that QFED emission estimates are based on an empirical relation between MODIS-retrieved fire radiative power and the total dry mass

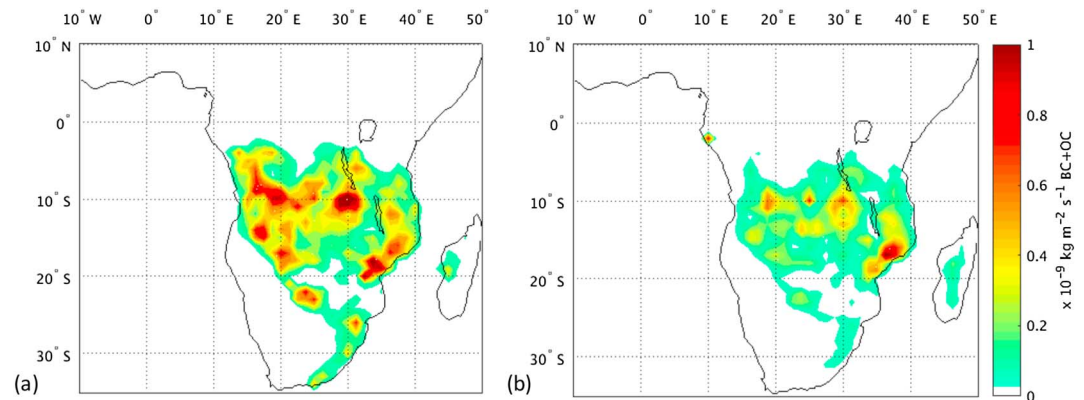


Figure 3. Input emissions of BC and OC ($\times 10^{-9} \text{ kg m}^{-2} \text{ s}^{-1}$) from (a) QFED2 and (b) GFED3 biomass burning inventory averaged over August and September 2008.

burned over the affected area (top-down approach), while GFED uses the properties of burning ecosystem along with the characteristics and extent of fires to estimate the amount of mass emitted for different aerosol species and trace gases during BB (bottom-up approach). The spatial distribution of combined BC and OC mass emitted over our domain from the two inventories is depicted in Figure 3, with regionally averaged emission totals of 0.02×10^{-9} and $0.04 \times 10^{-9} \text{ kg m}^{-2} \text{ s}^{-1}$ for GFED3 and QFED2, respectively. Model simulations with GFED3 emissions were particularly made to facilitate the comparisons of the long-range plume transport between GEOS-5 and other AeroCom models. GEOS-5-GOCART treats emission injection heights by assuming BB emissions to be uniformly distributed throughout the planetary boundary layer of the grid box in which fire emissions occur owing to the heat generated during burning [Colarco *et al.*, 2010].

2.2. AeroCom Models

The AeroCom project was created in 2003 to assemble outputs from various global aerosol models at a common platform to facilitate intermodel comparisons and model evaluations using observational data sets. The modelers are requested to follow a common data protocol and provide details about their respective model configurations depending on the objective of the proposed experiment for which they submit the results. Several studies have used outputs from AeroCom Phase I [Kinne *et al.*, 2006; Koffi *et al.*, 2012; Schulz *et al.*, 2006; Textor *et al.*, 2006] and Phase II experiments [Koffi *et al.*, 2016; Myhre *et al.*, 2013; Samset *et al.*, 2013] to evaluate the representation of aerosol emissions, lifecycle, optical properties, vertical distributions, or radiative forcing in the participating models. Further details of the experiments can be found at the main AeroCom website (aerocom.met.no).

For our study, we used the outputs from four state-of-the-art global aerosol models participating in the BB emissions experiment proposed under the AeroCom Phase III project (<https://wiki.met.no/aerocom/phase3-experiments>). Although the original objectives of the BB experiment are different from our study, the results from Stage I of the experiment are relevant to us, as it required the models to simulate the aerosol extinctions using the same BB emissions (GFED3). A similarity in emission inputs amongst the models makes the interpretations of model diversity in simulating vertical distributions of aerosols solely dependent on aerosol processing and transport. All the models were run for the complete year of 2008, of which we have used the data for only the peak BB months of August and September [Abel *et al.*, 2005]. The models considered in our study (Table 1) include atmospheric GCMs that used either MERRA (GEOS-5-GOCART) or ERA-Interim reanalysis data set (CAM5, HadGEM3, and ECHAM6-SALSA) to replay or constrain the model-simulated meteorological fields, and an offline CTM (GEOS-CHEM) that was driven using assimilated meteorological fields from GEOS-5 (GEOS-5-GMAO). Different emission injection height assumptions and moist convection schemes were used for different models, which are mentioned in Table 1. The table also lists other useful information about the configurations that models used to generate the simulations used in our study. The representation of aerosol dry and wet removal processes across the models is quite varied. The details about how each model treats these processes can be found in the references listed in Table 1 for the respective models.

Table 1. Models Used in This Study and General Information About Their Configuration

	Model					
	CAM5	HadGEM3	ECHAM6-SALSA	GEOS-CHEM	GEOS-5-GOCART	
Operating institution	PNNL/UWyo	Met Office, UK	Finnish Meteorological Institute	University of L'Aquila, Italy, and University of Athens, Greece	GSFC	
Type	Atmospheric GCM	Atmospheric GCM	Atmospheric GCM	Offline CTM	Atmospheric GCM	
Horizontal resolution (latitude × longitude)	1.9 × 2.5	1.25 × 1.875	1.9 × 1.9	4 × 5	1 × 1.25	
Vertical levels	30 (to 3.6 hPa)	85 (to 0.01 hPa)	31 (to 10 hPa)	72 (to 0.01 hPa)	72 (to 0.01 hPa)	
Meteorological fields	ERA-Interim	ERA-Interim	ERA-Interim	GEOS-5-GMAO	MERRA	
Injection heights for BB emissions	Uniformly mixed within 1 km above surface	Evenly distributed within 0–3 km	Between 0 and 6 km ^a	Uniformly mixed within model-calculated PBL	Uniformly mixed within model-calculated PBL	
Moist convection scheme	Shallow: <i>Park and Bretherton</i> [2009] and deep: <i>Zhang and McFarlane</i> [1995]	<i>Gregory and Rowntree</i> [1990] and <i>Derbyshire et al.</i> [2011]	<i>Tiedtke</i> [1989] and <i>Nordeng</i> [1994]	RAS [<i>Moorthi and Suarez</i> , 1992]	RAS [<i>Moorthi and Suarez</i> , 1992]	
Aerosol mixing state	Internally mixed ^b	Internally mixed ^c	Externally mixed	Externally mixed	Externally mixed	
BB aerosol refractive index (550 nm)	BC OC	1.95 + 0.79 <i>i</i> 1.53 + 0.006 <i>i</i>	1.75 + 0.44 <i>i</i> 1.5 + 0 <i>i</i>	1.85 + 0.71 <i>i</i> 1.53 + 0.006 <i>i</i>	1.75 + 0.45 <i>i</i> 1.53 + 0.006 <i>i</i>	1.75 + 0.44 <i>i</i> 1.53 + 0.006 <i>i</i>
Basic reference	<i>Liu et al.</i> [2012]	<i>Johnson et al.</i> [2016]	<i>Stevens et al.</i> [2013]	<i>Bey et al.</i> [2001]	<i>Colarco et al.</i> [2010]	

^aBB emissions are distributed in six layers extending from the surface to 6 km following *Dentener et al.* [2006].

^bInternal mixing for particles within the same size mode and external mixing for particles across the modes (Aitken, accumulation, and coarse); carbonaceous aerosols are all in the accumulation mode.

^cInternal mixing within five size modes (nucleation, Aitken insoluble, Aitken soluble, accumulation soluble, and coarse soluble).

3. Observational Data Processing

The CALIPSO (Cloud-Aerosol Lidar and Infrared Pathfinder Satellite Observations) satellite carrying the CALIOP lidar system was launched in April 2006 as part of the “A-train” constellation of Sun-synchronous satellites that cross the equator in the early afternoon around 1330 local solar time (LST) in ascending orbit and at 0130 LST in the descending node, with a 16 day repeat cycle. CALIOP measures the backscatter intensity and the orthogonally polarized components of the backscatter signal at two wavelengths, 532 nm and 1064 nm, with a very fine vertical resolution of 30 m within the troposphere. The lidar system has a small footprint of only about 70 m and the laser pulse repetition frequency of 20.16 Hz produces footprints every 335 m along the ground [*Hunt et al.*, 2009; *Winker et al.*, 2009].

The attenuated backscatter measurements are made available in the Level 1 CALIOP products after geolocation and calibration and then converted to useful geophysical parameters, such as backscatter and extinction coefficients, and layer optical depths, using a series of data processing algorithms [*Winker et al.*, 2009; *Young and Vaughan*, 2009]. The identified aerosol layers during the processing algorithm are further classified into six aerosol types using a model-based scheme [*Omar et al.*, 2009]. These are polluted continental, biomass burning (or smoke), desert dust, polluted dust, clean continental, and marine. A number of aerosol and cloud optical properties derived using the processing algorithms, aerosol classification information, and spatial location of aerosol and cloud layers, along with the surrounding meteorological conditions (e.g., temperature, pressure, or surface elevation) measured by the instrument, are made available to users through the CALIOP Level 2 Profile and Layer products. For our study, we have used Version 3.01 Level 2 5 km Aerosol and Cloud Profile products to obtain the mean extinction profiles of smoke aerosol, while the aerosol base and cloud top heights were obtained from the corresponding 5 km layer products.

The Level 2 data files also contain several quality control flags that can be used to screen out poor or highly uncertain data. The significance of these flags and the directions to use them are explained in *Winker et al.* [2013]. To briefly summarize, we have used cloud aerosol distinction (CAD) scores, extinction uncertainty values, atmospheric volume descriptors (AVD), and extinction quality control (QC) flags to filter our extinction data before averaging them or using them for any comparative analysis. CAD score is a measure of confidence in the classification of identified layers into aerosol or cloud, with negative values for aerosols and positive values for clouds [*Liu et al.*, 2009]. Therefore, observations with absolute CAD scores of only 20 or above were used. The extinction QC flags summarize the initial and final state of the extinction retrieval. During the execution of the algorithm to find a solution, the lidar ratio may be adjusted, but there is most confidence in

extinction solutions when the lidar ratio is unchanged during the retrieval process (extinction $QC = 0$) or if the retrieval is constrained (extinction $QC = 1$) [Young and Vaughan, 2009]. Hence, we used observations that had QC flags of either 1 or 0. The retrieval process may also fail sometimes because the iterative process did not converge to a solution. Under such conditions, an extinction uncertainty of 99.99 is assigned to indicate an unreliable solution. So, all observations with an uncertainty of 99.99 km^{-1} were also discarded. Additionally, all extinction observations with AVD indicating clean air were assumed to have zero extinction values (instead of fill values of -9999) while calculating the mean extinction profiles [Ford and Heald, 2012].

While assessing the above-cloud aerosol optical depth of biomass burning plumes retrieved from A-train sensors over the SE Atlantic, it was found that CALIOP's operational 532 nm retrievals were underestimated by a factor of 5 or even more compared to those from passive sensors like MODIS, OMI (Ozone Monitoring Instrument), and POLDER (Polarization and Directionality of Earth Reflectances) [Jethva *et al.*, 2014; Torres *et al.*, 2013]. At the same time, CALIOP 1064 nm retrievals when converted to 500 nm using POLDER's Ångström exponent (α) brought the lidar retrievals closer to other observations. Hence, we have used the CALIOP 1064 nm extinction retrievals for obtaining the mean smoke extinction profiles in our study. To convert the 1064 nm extinction retrievals to the model's output frequency of 550 nm, we calculated $\alpha = 1.8$ for the 440–1020 nm pair using Level 1.5 monthly mean AOD measurements from nine different AERONET sites (<http://aeronet.gsfc.nasa.gov>) over the BB source region of our domain. This is consistent with the Eck *et al.* [2013] study, where the values of α in the 440–870 nm ranged primarily from 1.7 to 2.0 with a mean of 1.85 over the same region. Additionally, we chose to use only the nighttime retrievals of CALIOP as opposed to using both daytime and nighttime retrievals because smaller signal-to-noise ratio (SNR) during the daytime due to noise from background solar illumination decreases CALIOP's detection sensitivity toward tenuous aerosol layers, resulting in low-biased AOD values [Meyer *et al.*, 2013; Winker *et al.*, 2013].

To examine the long-range transport events that happen on timescales of several days, the limited spatial coverage of satellites with small footprints like CALIOP makes it difficult to determine the broad characteristics of the plume transport. Therefore, to ensure a better representation of the regional climatology, we obtained a gridded product of CALIOP data by aggregating the smoke extinction profiles (at 550 nm, converted from 1064 nm) for the peak biomass burning months of August and September from 2007 to 2009 onto global $2^\circ \times 2^\circ$ latitude-longitude grids. The median of the total number of valid CALIOP 5 km profiles per grid cell was 565, with maximum and minimum values of 1047 and 397, respectively. Further, the variation in the number of valid CALIOP observations with decreasing altitude up to the cloud or surface levels was found to be negligible over most parts of the domain compared to the total number of valid retrievals made at each level. The use of multiyear averages of observational data instead of exactly matching satellite and model data seems a reasonable decision for our case because we found low interannual variability in the magnitudes and shape of the smoke extinction profiles over our domain for the time period of averaging [see also Koffi *et al.*, 2012].

4. Results and Discussion

GOCART was run “online” with GEOS-5 in replay mode for the complete year of 2008 using a model configuration described in section 2. During the analysis and discussions in the subsequent sections, note that the mean of the model output quantities always represents an average over August and September 2008, while that for CALIOP represents an average over the same months but from 2007 to 2009. Since the temporal range of the CALIOP and model data does not overlap exactly, we do not intend to perform a detailed quantitative analysis of magnitudes of aerosol extinctions or optical depths but rather compare the broad features of aerosol spatial distribution and transport simulated by the models relative to CALIOP retrievals. The GEOS-5-simulated smoke extinctions in our analysis refer to the sum of extinctions for BC and OC components in the model, assuming that the contribution of anthropogenic BC and OC toward the total BC and OC over our domain and study period is negligible [Streets *et al.*, 2009]. For the AeroCom models, smoke extinctions were obtained as a difference between aerosol extinctions from two sets of similar simulations, one with the BB emissions and the other without them.

4.1. Smoke Aerosol Optical Depth and Cloud Spatial Distribution

Although the emphasis in this study is on the vertical distribution of BB aerosol, we begin with the examination of smoke aerosol optical depths and cloud fractions from satellite observations and model simulations to

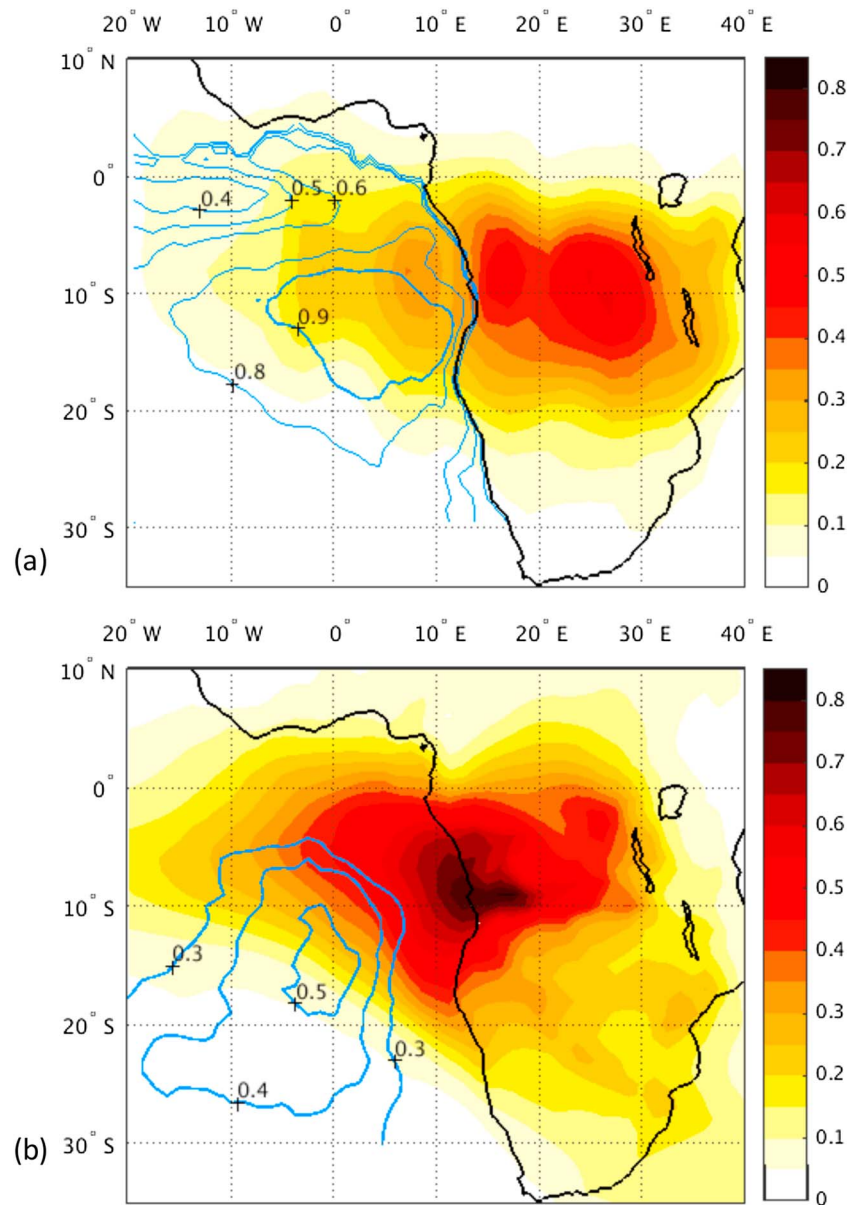


Figure 4. (a) Horizontal distribution of BB AOD (colored contours) from CALIOP gridded product (described in section 3) and low-level cloud fractions (blue line contours) from MODIS Level 3 monthly global product (MOD08_M3) for August–September 2008 and (b) corresponding results from GEOS-5 simulations using QFED2 BB emissions.

understand the general characteristics of the smoke and cloud spatial distribution in the region. The mean smoke AOD from CALIOP (Figure 4a) was derived by integrating the smoke extinction values from our gridded product (described in section 3) over all the CALIOP levels. The gridded AOD product was smoothed using a convolution filter for plotting purposes to facilitate the visualization of the spatial pattern of the underlying data. The low-level cloud fractions, depicted by the blue line contours in Figure 4a, were obtained from Level 3 MODIS Atmosphere Monthly Global Product (MOD08_M3) at 1° spatial resolution for August–September 2008. The corresponding cloud fractions and mean smoke AOD simulated by GEOS-5 (using QFED2 emissions) are shown in Figure 4b.

In general, the gradual decrease in the magnitudes of smoke AOD starting from the burning source region to the west of the continent for both modeled and CALIOP data is consistent with our understanding of the directions of smoke outflow for the savannah fires. However, some noticeable differences in the horizontal distribution of modeled and observed smoke AOD over the continent are also evident. For example, there

Table 2. Mean Smoke AOD Estimates From GEOS-5 Model, CALIOP, and Previous Study

Aerosol	Land AOD	Ocean AOD
GEOS-5 smoke (using QFED2 emissions)	0.30	0.28
GEOS-5 smoke (using GFED3 emissions)	0.15	0.12
CALIOP smoke	0.30	0.14
MODIS ^a	0.38 ^b	0.16 ^c
CAM3-Slab Ocean Model ^a (carbonaceous)	0.27	0.14

^aClimatological mean over July–October (2001–2008) [from *Sakaeda et al.*, 2011].

^bMODIS total AOD.

^cMODIS fine-mode AOD.

is an area of high AOD values observed by CALIOP between 10°–15°S and 25°–30°E, which seems to be missing (or misplaced) in GEOS-5 simulations. Interestingly, this area of high AOD values retrieved by CALIOP corresponds to the large fire pixel counts observed by MODIS (Figure 1) and relatively high values of QFED2 estimated emissions (Figure 3a) around the same region. One of the probable reasons of this discrepancy could be the quick outflow of smoke plumes from the intense burning source toward the north of the continent due to the occurrence of high wind speeds over this area in the model, along with the formation of a confluence north of this region (shown by MERRA wind streamlines in Figure 8b).

The low-level cloud fractions from MODIS are also significantly different from those simulated by GEOS-5 in terms of both magnitudes and spatial distribution. The MODIS clouds appear to be hugging the western coast of the continent and extend into the deep ocean with cloud fractions greater than 0.9 between 5°S and 20°S. The GEOS-5 clouds, on the other hand, appear to be more southward and farther away from the coast compared to MODIS clouds, with maximum cloud fraction values of only about 0.5. Having knowledge of this discrepancy might be important because the spatial location of clouds is related to the convective activity occurring at these locations. This inability of reproducing realistic stratocumulus cloud decks off the western coasts of the continents has been found to be a common problem for most of the global models that have participated in previous AeroCom experiments too [*Stier et al.*, 2013].

To establish the reasonableness of the modeled and observational data used in our study, we compare the mean smoke AOD estimates from GEOS-5 and CALIOP with those from a previous study [*Sakaeda et al.*, 2011] that was based over the same region of interest as ours (Table 2). We calculated the mean AOD separately for the land (0–20°S, 13°E–40°E) and the oceanic (0–20°S, 13°E–20°W) parts of the domain to allow for a fair comparison with the previous study. However, it should be noted that the observational and model estimates from *Sakaeda et al.* [2011] are climatological means from 2000 to 2008 for the entire dry season of July–October. Table 2 shows that the mean smoke AOD derived using our CALIOP gridded product falls within ~20% of mean MODIS total AOD over land and within ~10% of mean MODIS fine-mode AOD over the ocean. MODIS fine-mode AOD over land was intentionally not included in our comparisons because the use of this product for evaluation studies is not recommended [*Levy et al.*, 2010]. The close agreement of CALIOP and MODIS AOD estimates reemphasizes that retrievals of CALIOP extinctions or AOD at 1064 nm are more suitable for evaluation of model simulations instead of the standard AOD retrievals at 532 nm, which have been found to be underestimates by about a factor of 5 or more over this region [*Jethva et al.*, 2014]. Although all the estimates of mean smoke AOD over land in Table 2 fall within 20% of GEOS-5 simulated AOD (using QFED2), the AOD gradient from land to ocean for GEOS-5 is quite low (~10% decrease) compared to the other estimates in the table. The reduction in AOD from land to ocean is ~50% for CALIOP and the CAM3-Slab Ocean Model. The former might be an overestimate because CALIOP cannot retrieve the smoke aerosol lying below the clouds over the ocean. Between the models (GEOS-5 and CAM3), however, the differences in AOD gradients can be partly attributed to the use of different BB emissions for each of the models. In fact, QFED2 BB emissions show the presence of heavy fires concentrated along the western coastline of the continent (Figure 3a), which in conjunction with the prevailing high winds in the model contribute to the high AODs over the ocean and land for GEOS-5.

4.2. Contrast in Extinction Profiles Over Land and Ocean

4.2.1. Sampling Along CALIPSO Tracks

We compared smoke extinctions at 532 nm retrieved from the standard CALIOP Level 2 layer product with GEOS-5-GOCART-simulated smoke extinction coefficients at 550 nm along nighttime CALIPSO satellite

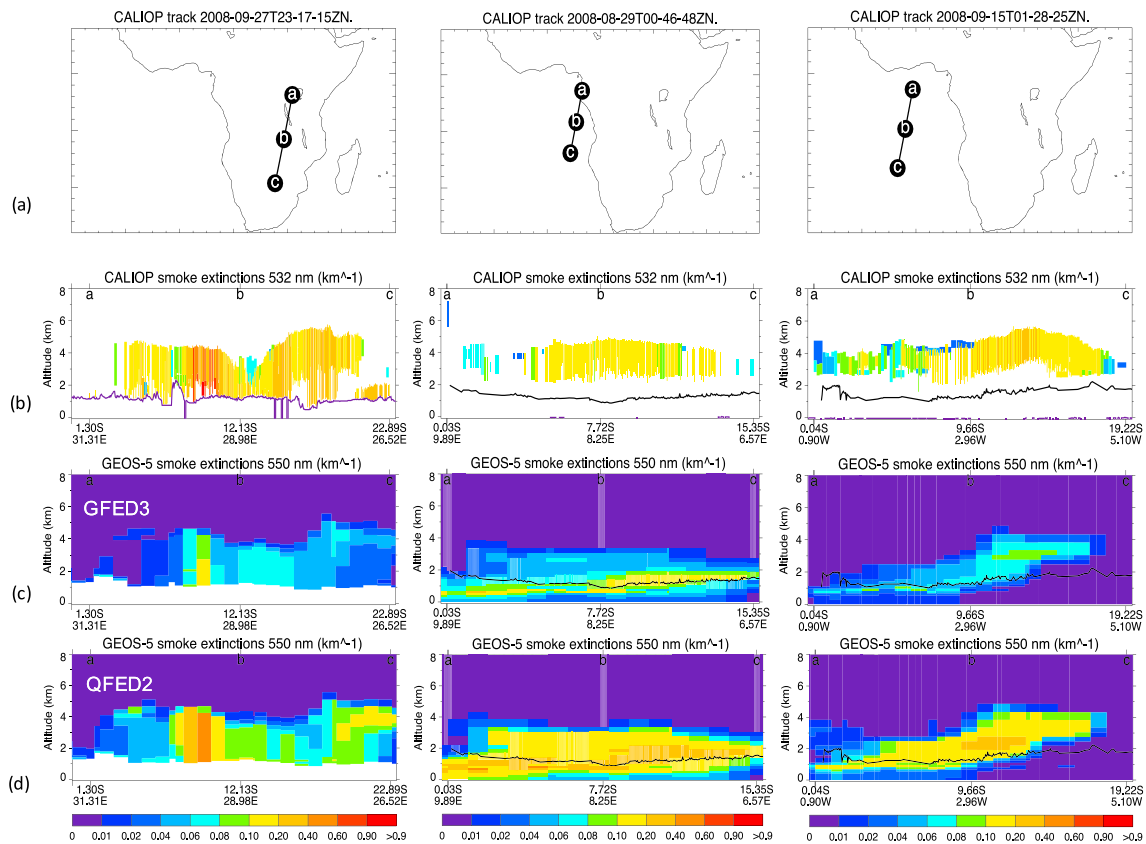


Figure 5. Vertical distribution of smoke aerosol extinctions (km^{-1}) along (a) three distinct CALIPSO satellite tracks retrieved from (b) CALIOP at 532 nm and those simulated by GEOS-5-GOCART at 550 nm (c) using GFED3 BB emissions and (d) using QFED2 BB emissions. CALIOP-retrieved cloud top heights are depicted using black lines on both CALIOP and GEOS-5 panels for tracks over the ocean. CALIOP-observed surface elevation is plotted (in purple) on CALIOP panel for the track over land. White region on CALIOP panels represents no detectable signals of smoke aerosol.

tracks over our domain to evaluate the vertical distribution of smoke aerosol in the model at different stages of the plume transport. There were typically two to three nighttime CALIPSO tracks every 24 h that passed over our domain. We also used these comparisons to examine the sensitivity of the model-simulated extinctions toward the use of different BB emissions. The matching of the model and CALIOP data was done by choosing the instantaneous extinction values from the 3-hourly generated model output file that was closest to the time of CALIPSO overpass. Figure 5 shows three such satellite tracks that cut across the primary direction of plume transport and are representative of the typical scenarios we observed at three distinct locations during most of the days of the BB months. The first track (from left) runs along the BB source region; the second is just off the western coast, where the plume transitions from land to the ocean; and the third track is further offshore, where the plume comfortably resides above the stratocumulus cloud deck.

The variations in the smoke layer top altitudes (~ 3.5 to 4.5 km above ground elevation) along satellite tracks over the BB areas on land (left panels of Figure 5) are, in general, captured by the model. However, for the CALIPSO tracks passing along the coast and further into the ocean (middle and right panels of Figure 5), some remarkable differences between the vertical distribution of the model simulated and CALIOP retrieved smoke layers exist. CALIOP observes smoke layer top heights over the ocean at ~ 4 to 5.5 km above sea level (asl), and the layer base heights are detected mostly above 2.5 km asl. In contrast, the bulk of the model-simulated smoke layers appears to be residing at lower altitudes than CALIOP. The difference between CALIOP and model-simulated layer top heights is between 1 and 1.5 km in the areas adjacent to the coast (middle panels of Figure 5), but this difference can increase up to ~ 2 km for satellite tracks far away from the coast and between 0 and 10°S (right panels of Figure 5). The occurrence of smoke aerosol layers at elevated altitudes above the MBL, mostly between 2 and 6 km asl, was also observed during the Southern African Regional

Science Initiative (SAFARI 2000) [Haywood *et al.*, 2004] and other in situ aircraft measurements over the ocean in this region [Anderson *et al.*, 1996; Kaufman *et al.*, 2003].

The relative locations of the CALIOP smoke extinctions (color filled) and cloud top heights (black line) over the ocean (middle and right panels of Figure 5) suggest that CALIOP smoke layers reside well above the cloud levels with a persistent “clear air” gap (in white) between the base of the CALIOP smoke layers and top of the cloud decks. The CALIOP estimates of this gap, however, can be biased at times due to the overestimation of the aerosol layer base heights by the standard feature detection algorithm of CALIOP [Liu *et al.*, 2015; Painemal *et al.*, 2014]. This bias can occur in CALIOP measurements when the backscatter intensities fall below the detection thresholds [Vaughan *et al.*, 2009] or CALIOP signal is substantially attenuated in areas of optically thick aerosol layers. The bias due to signal attenuation is further discussed in section 4.3.2. Nonetheless, since the magnitudes of aerosol extinction decrease as the smoke plumes move away from the burning sources (Figure 4), we can expect the effects of strong signal attenuation over the ocean to be most prevalent for the smoke layers adjacent to BB sources along the coast and up to about 0°. Therefore, for other parts of the ocean, the clear gap between the smoke and cloud layer might possibly be true or at most reflects the presence of weakly scattering aerosols within this gap. In fact, observations of aerosol and cloud vertical distributions along the flight tracks off the coasts of Namibia and Angola and also around Ascension Island (~2500 km away from the west coast) during SAFARI 2000 also suggested that the cloud tops were mostly separated from the overlying BB smoke layers by “clean air slots” [Haywood *et al.*, 2004, and references therein].

The comparisons along satellite tracks and mean smoke AOD estimates from Table 2 show that by using different BB emission inventories (QFED2 and GFED3), the GEOS-5 AOD values can be changed by about a factor of 2 and the model-simulated extinction or AOD values are closer to those from CALIOP when QFED2 emissions are used. However, the horizontal and vertical locations of the smoke aerosol in the model are unaffected by the use of either of the emission inventories. Thus, for the discussions hereafter, GEOS-5 model output represents results from the QFED2 simulations unless otherwise specified.

4.2.2. Mean Extinction Profiles

The contrast in the GEOS-5 performance in simulating aerosol vertical distribution over the burning source region versus the smoke outflow region is further examined by comparing the mean smoke extinction profiles from GEOS-5 and CALIOP separately for the land and oceanic part of the domain (Figure 6). The mean cloud extinction profiles retrieved from CALIOP are also plotted along with the smoke extinction profiles for the subplots over the oceanic region to visualize the vertical location of the smoke layer relative to that of the stratocumulus cloud deck. It should be noted here that we have replaced the “clean air” retrievals of CALIOP with zero extinction values, which are also accounted for while evaluating the mean aerosol or cloud extinctions at each CALIOP vertical level. Thus, the mean extinction value at a particular level for either aerosol or cloud is a resultant of both the frequency of occurrence and the magnitude of extinctions observed at that level. To avoid averaging out the distinct patterns of aerosol transport or vertical distribution that could possibly exist for different regions within the domain, we make the comparisons here and also during all subsequent analysis for three subregions (Figure 2) of equal width (10° latitude) extending from 35°E to 15°W.

Over land, the model and CALIOP mean extinction profiles are in reasonable agreement with each other with respect to the shape of the profiles. The magnitudes of GEOS-5 extinctions, however, are underestimated for subregion B (up to about 40%) and overestimated for subregion A (up to about 70%) compared to CALIOP extinctions. Over ocean, the area under the extinction curve, which can be considered as a proxy for the column aerosol load, is much higher for GEOS-5 compared to CALIOP for all the subregions. The overlap of CALIOP smoke and cloud extinction profiles between ~1.5 and 2.2 km asl in subregions B and C depicts the possibility of instances when the bottom of the smoke layer comes in physical contact with the cloud tops [Costantino and Bréon, 2013]. The model-simulated smoke extinction profiles are in closest agreement with the CALIOP profiles for subregion A in terms of the profile shape and altitude of peak extinction (2.5 km for GEOS-5 versus 3.5 km for CALIOP), although the magnitudes of extinctions are lowest for this subregion compared to the entire domain. The peak of the model-simulated smoke aerosol extinction profiles occurs at levels 1–2 km lower compared to the peak of the CALIOP-retrieved smoke extinction profiles for all the three subregions. For subregion C, the peak of the model smoke extinction profile is most displaced from that of CALIOP (at ~3.5 km) and interestingly coincides with the peak of the CALIOP cloud extinction profile (at ~1.5 km). However, it is also important to note that high relative humidity at cloud levels in the model can

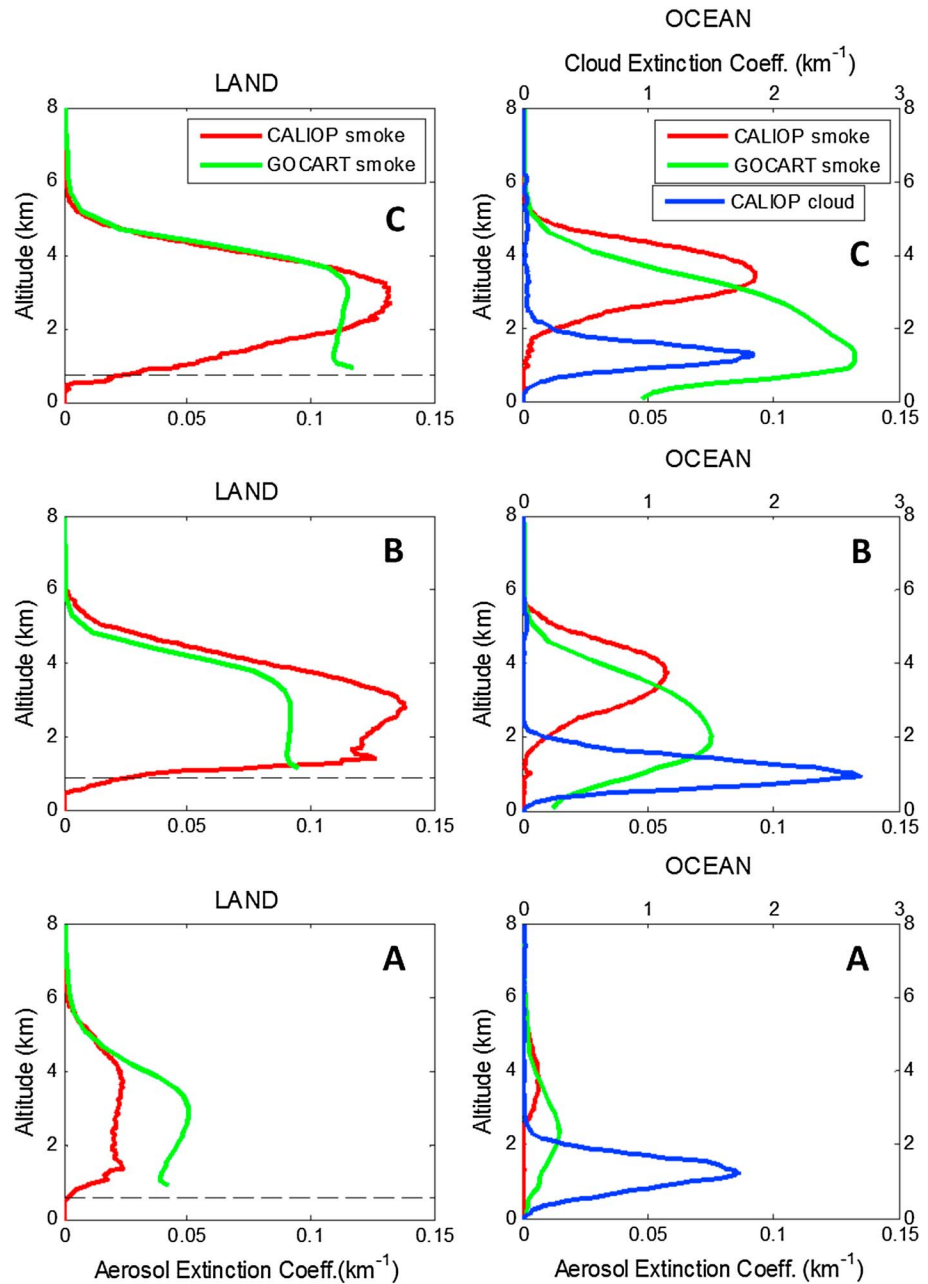


Figure 6. Comparisons of mean (August–September) smoke extinction profiles (km^{-1}) from CALIOP (in red) and GEOS-5-GOCART (in green) over land (13° – 35° E) and oceanic (13° E– 15° W) parts of the three subregions, viz., A (30° – 20° S), B (20° – 10° S), and C (10° S– 0°) of the domain. CALIOP-retrieved cloud extinction profiles (in blue) are plotted using the upper x axis for profiles over the ocean to show relative altitudes of smoke and cloud layers. The mean surface elevations retrieved from CALIOP are shown using dashed lines on profiles over land.

also contribute to an increase in aerosol extinction values at these levels. Thus, the increase in modeled aerosol extinctions at these levels does not necessarily imply a proportionate increase in the amount of aerosol at these levels.

4.3. Aerosol Plume Transport

4.3.1. Multimodel Evaluation

We evaluated the plume transport features simulated by GEOS-5 and other AeroCom models with those from CALIOP to note the discrepancies between observed and simulated aerosol transport that might be common

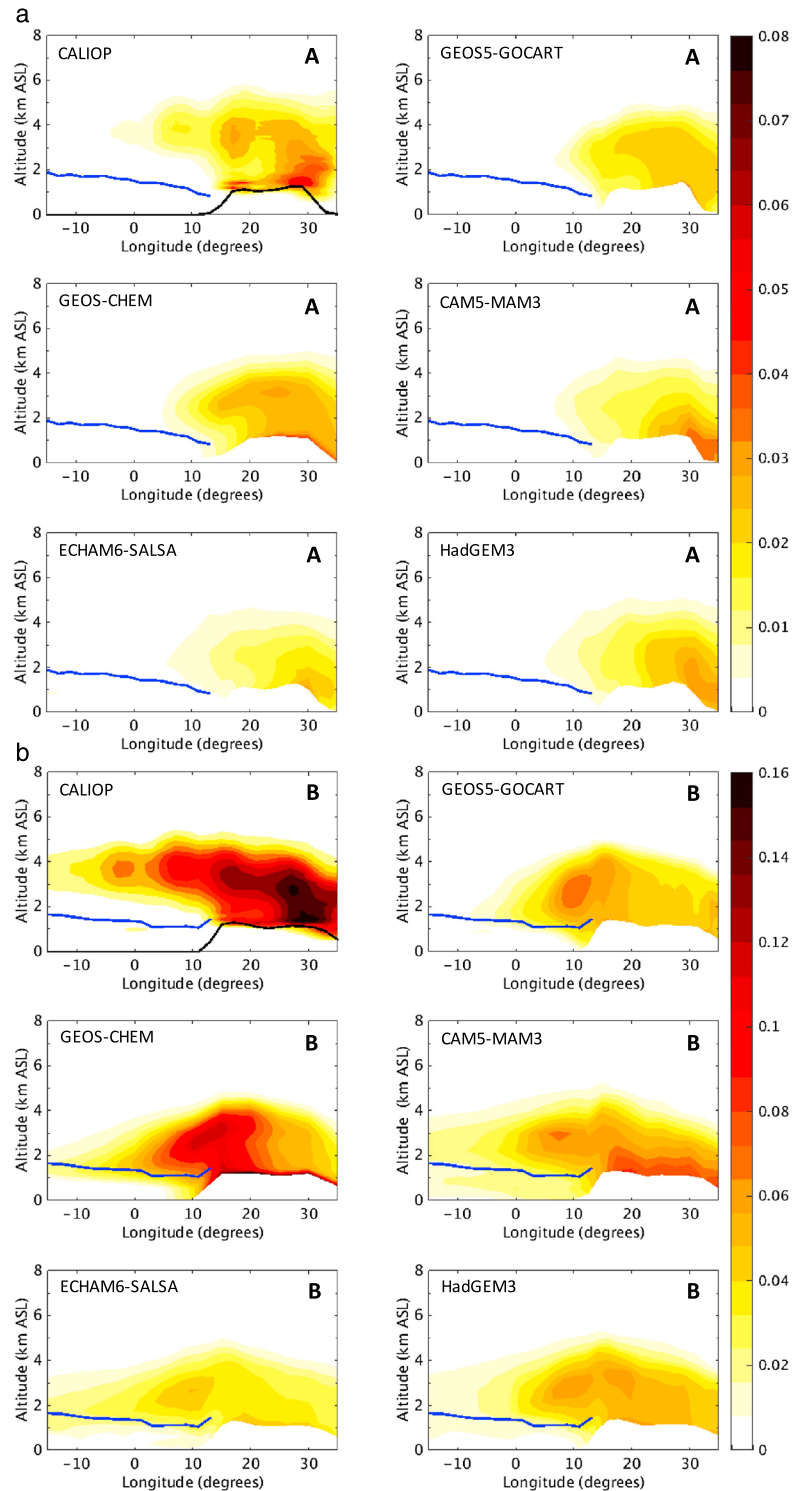


Figure 7. (a) Meridional average of smoke aerosol extinction coefficients (km^{-1}) over subregion A (30° – 20° S, 35° E– 15° W) from CALIOP, GEOS-5-GOCART, and the four AeroCom models (GEOS-CHEM, CAM5, ECHAM6-SALSA, and HadGEM3). CALIOP-retrieved mean cloud top heights are overlaid (in blue solid line) on all the panels for the oceanic parts of the domain. The black solid line on the CALIOP panel depicts the mean surface elevation measured by the lidar signal. Note that all models used the GFED3 BB emission inventory and model averages are for August–September 2008, while CALIOP averages are for August–September 2007–2009. (b) Same as Figure 7a but over subregion B (20° – 10° S, 35° E– 15° W). (c) Same as Figure 7a but over subregion C (10° S– 0° , 35° E– 15° W).

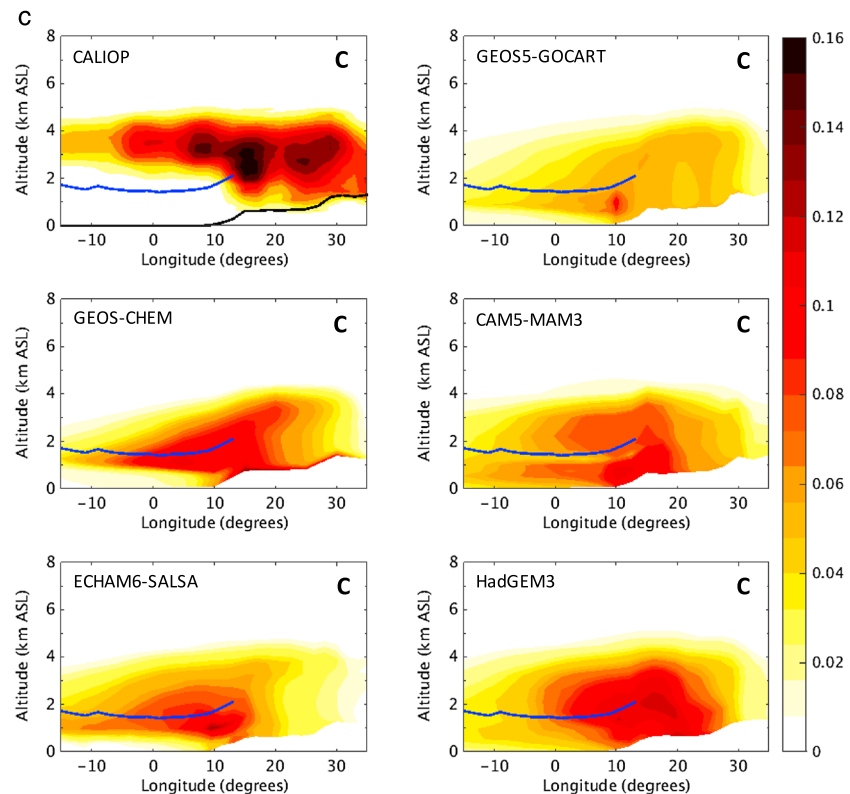


Figure 7. (continued)

to most of the global models in this important region of BB. Contours of meridional mean smoke aerosol extinctions along the longitude height cross sections (Figures 7a–7c) illustrate the transport and transformation of the aerosol plume from land to the ocean. The GEOS-5-simulated extinctions here are based on GFED3 BB emissions, same as that for other models to make the intermodel comparisons equitable. The CALIOP-retrieved mean cloud top heights (in blue) are superimposed over the filled contours of aerosol extinctions to understand the variations in relative altitude of cloud tops with respect to smoke layers. The Figures 7a–7c are accompanied by Table 3 that contains the mean AOD between 2 and 4 km asl (AOD_{2-4}) from CALIOP and the models averaged over three 10° longitude-by-latitude boxes, wherein each box represents a different stage of smoke plume in the direction of its transport. The first latitude-longitude row (or box) for each subregion refers to the land region adjacent to the ocean (20° – 10° E). The second row refers to the oceanic region adjacent to the continent (10° E– 0°), and the third row refers to the oceanic region farther offshore (0° – 10° W). Vertical levels between 2 and 4 km were chosen for calculating the mean AOD because CALIOP cannot measure aerosol below cloud levels and maximum cloud top heights occur at ~ 2 km over the ocean. Since most models considered in this study used MERRA and ERA-Interim wind fields, the horizontal wind streamlines (Figure 8) and vertical pressure velocities (Figure 9) from the two data sets were obtained to understand the observed similarities or differences in the horizontal and vertical transport of aerosol plumes amongst the models due to large-scale motion. Since CALIOP data in our study are the mean over 2007–2009 and the model results are for 2008 only, we also compared the MERRA data for each of the 3 years to assess the representativeness of the year 2008 in terms of the transport pattern over our domain. The results (not shown here) showed very low interannual variability in the directions of wind streamlines and magnitudes of wind speeds and vertical pressure velocities. In addition, the horizontal wind fields from MERRA and ERA-Interim were quite similar, so only the MERRA wind streamlines are depicted in Figure 8 to avoid redundancy.

Some transport features are common to all the three subregions of the domain. For example, the maximum heights up to which the smoke aerosol plumes get lofted over land (~ 3.5 to 4.5 km above ground elevation) are well captured by all the models when compared to CALIOP observations (Figure 7), irrespective of the

Table 3. Mean Aerosol Optical Depth Between 2 and 4 km Above Sea Level (AOD_{2–4}) From Models and CALIOP Averaged Over Three 10° Longitude-by-Latitude Boxes in the Direction of Aerosol Plume Transport for Each Subregion

Subregions		CALIOP	GEOS-5	GEOS-CHEM	CAM5	ECHAM6	HadGEM3
A (30°–20°S)	(20°E–10°E)	0.04	0.04	0.04	0.02	0.02	0.02
	(10°E–0°)	0.02	0.01	0.01	0.01	0.01	0.01
	(0°–10°W)	0.01	0.00	0.00	0.00	0.00	0.00
B (20°–10°S)	(20°E–10°E)	0.22	0.12	0.20	0.11	0.08	0.11
	(10°E–0°)	0.13	0.06	0.10	0.10	0.07	0.09
	(0°–10°W)	0.08	0.02	0.03	0.05	0.03	0.04
C (10°–0°S)	(20°E–10°E)	0.27	0.10	0.14	0.14	0.11	0.19
	(10°E–0°)	0.19	0.07	0.08	0.12	0.12	0.16
	(0°–10°W)	0.12	0.04	0.04	0.08	0.08	0.10

differences in emission injection heights assumptions amongst them (Table 1). This may be attributed to the strong uplifting over land surfaces (Figure 9) in the models. More importantly, CALIOP-observed smoke aerosol plumes transition from land to the ocean only at elevated levels above the MBL and maintain the peak of the smoke extinction profiles between 3 and 4 km asl throughout their course of transport over the ocean. This behavior of CALIOP aerosol plumes can be correlated with the directions and magnitudes of the horizontal winds in the region (Figure 8). The easterlies directed from the polluted air mass over land prevail at altitudes greater than or equal to 2 km (~800 hPa). At levels below 2 km, the winds over the ocean are directed from the southeast, where clean maritime air masses reside. Also, strong wind speeds across the land-ocean boundary seem to exist between 700 and 600 hPa (3–4 km asl), with wind speed maxima of ~7–8 m/s occurring around 650 hPa. In contrast to CALIOP observations, model-simulated aerosol plumes rapidly descend to lower levels over the ocean relative to the heights up to which they were lofted over land. This may be attributed to the strong downward motion over the ocean in the models (Figure 9), causing the aerosol plumes to experience a sudden subsidence as they transition from land to the

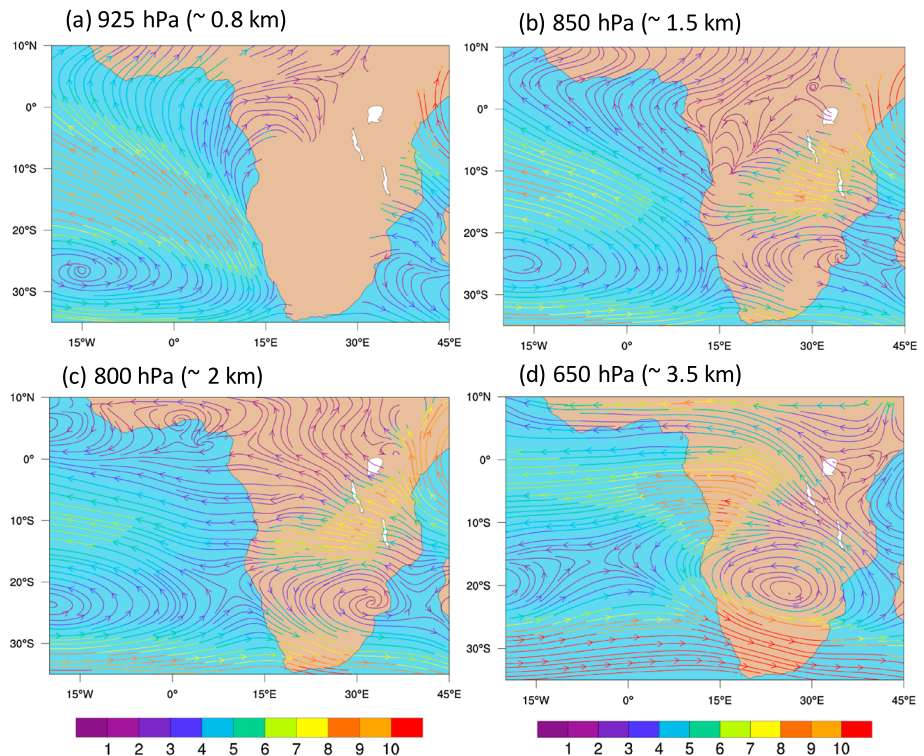


Figure 8. Horizontal wind streamlines over the domain at significant pressure levels, retrieved from MERRA reanalysis data and averaged over August–September 2008. The streamlines are colored by the wind speeds in m/s.

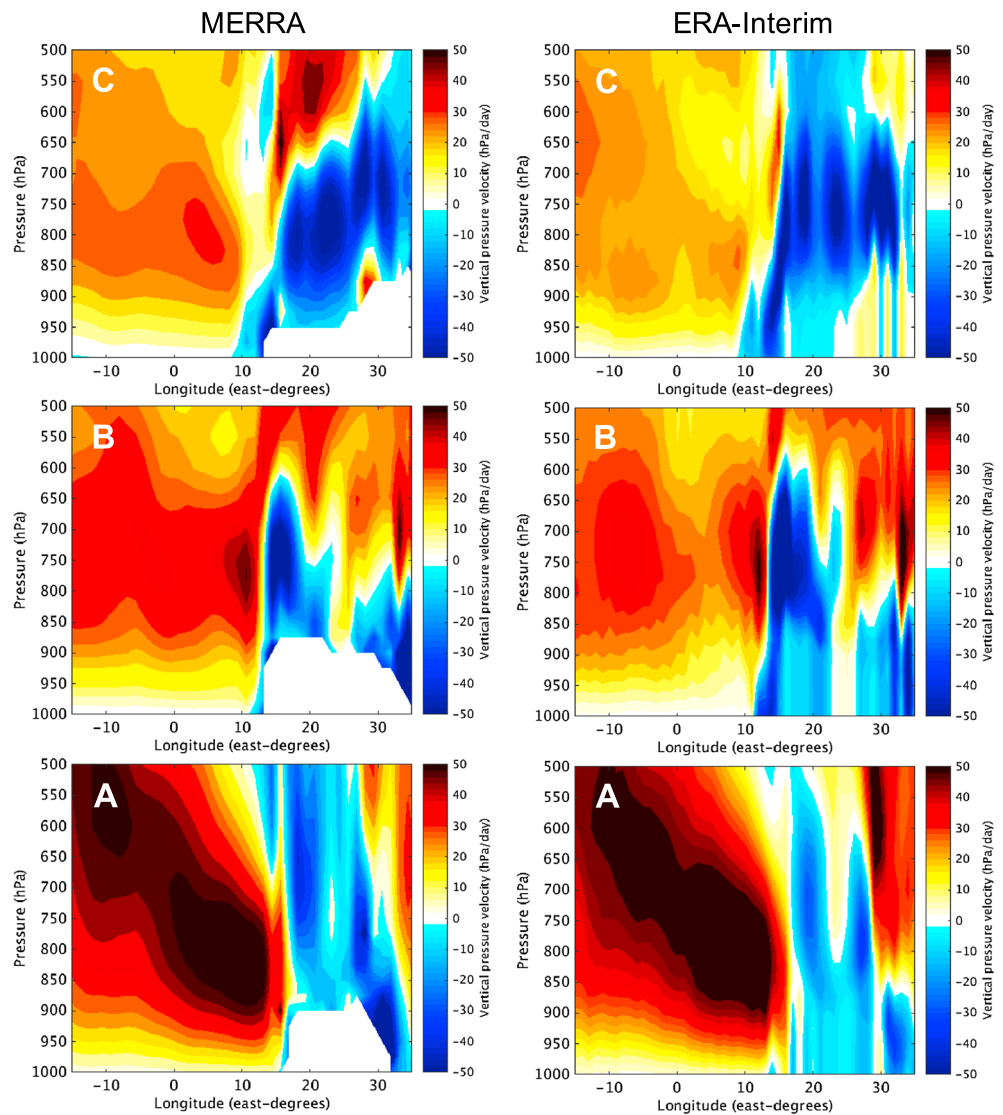


Figure 9. Vertical pressure velocities (hPa/d) during August–September 2008 from (left column) MERRA and (right column) ERA-Interim reanalysis data over the three subregions of the domain. Warmer colors signify downward motion, while cooler colors signify upward motion.

ocean. However, the levels to which the aerosol plumes get subsided and the steepness of this aerosol descent vary amongst the models and also amongst the different subregions in the domain.

In subregion A (Figure 7a), high extinction values near the land surface occurring between 30° and 35°E in all the model and CALIOP subplots represent BB sources along the east coast of the continent (Figure 1). However, only a small fraction of the smoke aerosols originating from this source makes it to the west coast across the Namib Desert and farther into the Atlantic Ocean, also depicted by the near-zero values in the third row of Table 3 for subregion A. This is because the horizontal winds in this region deflect the westward traveling smoke plumes toward the southeast direction (Figures 8c and 8d). For the aerosol particles that do reach the Atlantic though, their descent to the lower levels across the land-ocean boundary is not very drastic in the models and aerosol plumes manage to stay well above the observed cloud levels during their further transport.

Over land in subregion B (Figure 7b), discrepancies in the spatial locations of the intense burning sources between the model simulations and CALIOP observations are evident. The locations of intense burning sources can be recognized in the contour plots when very high smoke extinction values compared to its

neighboring regions occur at levels near the land surfaces and continue up to the levels to which smoke plumes are lofted. For example, it can be clearly seen that plumes start from a band between 30° and 20°E in CALIOP observations, while in all the models, except CAM5, the elevated plumes are visible only near 20°E. Recall our previous discussion in section 4.1 about the missing area of very high AOD values in GEOS-5 around the same locations. One of the probable reasons could be weak uplifting in the models near 30°E (Figure 9) but strong horizontal winds directed northward just above the land surface (800 and 850 hPa in Figure 8) in this area. The weak uplifting in CAM5 though may partly be compensated by the strong convective mass fluxes occurring around the same region, shown in Figure 13.

Over the ocean in subregion B, simulated aerosol transport in GEOS-5 and GEOS-CHEM is characterized by a sharp descent of aerosol plumes from ~4 to 5 km asl down to the levels near the observed cloud tops, noticeably between 12° and 0°E (Figure 7b). However, for models using ERA-Interim wind fields (CAM5, ECHAM6, and HadGEM3), the slope of this descent is not so steep. This is also reflected in the AOD₂₋₄ gradient between the first and second row of Table 3 (~50% decrease for GEOS-5 and GEOS-CHEM as opposed to only ~10–15% decrease for the other models). During further transport of smoke plumes from the coast to the deeper parts of the ocean, CAM5 stands out compared to the other models with respect to maintaining the peak of smoke extinctions at 2–3 km asl (compared to 3–4 km asl for CALIOP smoke) and having the highest AOD₂₋₄ between 0 and 10°W compared to the other models (Table 3). Another characteristic difference between CALIOP retrievals and the model simulations in this subregion lies in the estimation of magnitudes of aerosol extinctions. Simulated smoke extinctions by all the models except GEOS-CHEM are lower by a factor of 2 or more compared to CALIOP extinctions, even though all the models used the same BB emissions input from GFED3 (see the first row for subregion B in Table 3 and Figure 7b). This anomalous behavior of GEOS-CHEM could possibly be a resultant effect of the following factors. GEOS-CHEM has a much coarser horizontal resolution compared to other models (Table 2), which can affect its simulation of vertical processes [Protonotariou *et al.*, 2010]. Differences in assumptions of aerosol optical properties and size distributions can also cause substantial differences in estimation of aerosol extinctions [Curci *et al.*, 2014]. Further investigation into the relative contribution of each of these factors in causing this strikingly different extinction magnitudes simulated by GEOS-CHEM is beyond the scope of this paper.

In subregion C (Figure 7c), the plume transport features are quite varied amongst the models. The surface elevation at the coasts (~0.5 km asl) here is much lower than the layer top heights of the clouds (~2 km asl) residing along the coasts. So there is a high possibility that smoke aerosol originating from the burning areas near the coast gets advected into or below the clouds. Since CALIOP cannot detect aerosol below the cloud layers, it is not possible to estimate the fraction of smoke aerosol occurring below the cloud levels compared to the fraction of smoke aerosols occurring above the clouds. Previous studies [Costantino and Bréon, 2013; Painemal *et al.*, 2014] have also found evidence of large microphysical changes in the clouds over this subregion (mainly north of 5°S) owing to the presence of aerosols within the clouds. CALIOP observes a thick smoke layer above the clouds with a narrower clean air gap between the smoke and cloud layers compared to the other parts of the domain, but with the peak smoke extinctions still occurring between 3 and 4 km asl. Amongst models, the ones using ERA-Interim meteorological fields (CAM5, ECHAM6, and HadGEM3) are able to keep a substantial amount of aerosol above the observed cloud tops over the ocean, resulting in simulated AOD₂₋₄ values to be ~65–85% of CALIOP observed AOD₂₋₄ values for both near and farther offshore areas (Figure 7c and Table 3). For GEOS-5 and GEOS-CHEM, however, the bulk of the aerosol layer over the ocean stays much lower compared to CALIOP, especially farther offshore between 0 and 10°W, where AOD₂₋₄ for both the models is merely ~30% of the CALIOP-observed AOD₂₋₄ value of 0.12 (Table 3). This may be partly attributed to the differences in vertical velocities between MERRA and ERA-Interim for this subregion. The subsidence over the ocean in MERRA is much stronger (~30–40 hPa/d) than that of ERA-Interim (~10–20 hPa/d) here (Figure 9).

4.3.2. CALIOP Measurement Biases

Although we compared the model simulations with CALIOP observations to evaluate the smoke plume transport in the models, we are also aware of the inherent limitations of CALIOP that should be discussed in the context of our region of interest to explain some of the discrepancies in the spatial locations of aerosol between the model simulations and CALIOP observations. For example, the presence of intense burning sources near the coasts around 20°E (Figure 1) in subregion B is captured by all the models in Figure 7b but is less prominent in CALIOP observations. This shortcoming of CALIOP retrievals can be attributed to

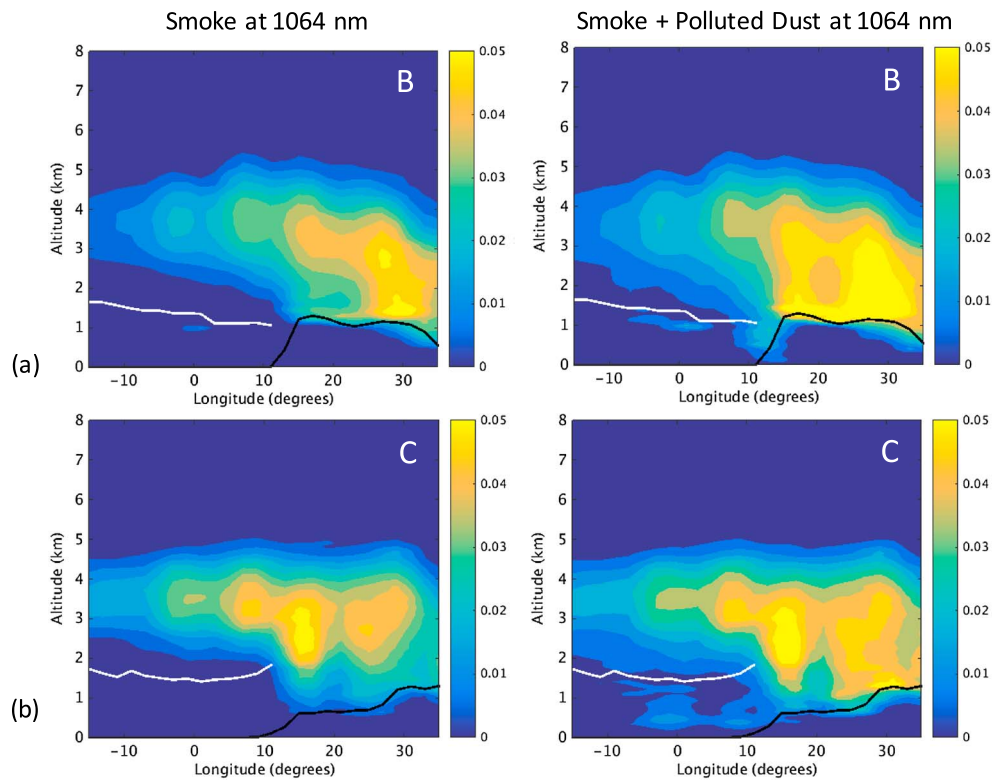


Figure 10. Comparison of CALIOP-classified smoke (left) and smoke plus polluted dust (right) aerosol extinction coefficients (km^{-1}) at 1064 nm over subregions (a) B (20°S – 10°S , 35°E – 15°W) and (b) C (10°S – 0° , 35°E – 15°W). CALIOP-retrieved mean cloud top heights are superimposed in white over the ocean.

substantial attenuation of the lidar signal by optically thick aerosol layers existing above the burning sources. The signal can at times be completely attenuated at levels within the aerosol layer, leading to no further retrievals below those levels. At other times, however, the reduction in SNR (signal-to-noise ratio) due to signal attenuation may lead to misclassification of aerosol type within the aerosol layers [Kacenenbogen *et al.*, 2014] by the CALIOP aerosol classification algorithm [Omar *et al.*, 2009]. In fact, when CALIOP observations were compared with those from High Spectral Resolution Lidar (HSRL-1) [Burton *et al.*, 2013] and AERONET [Mielonen *et al.*, 2009] in terms of aerosol subtype classification over other regions of BB pollution, results showed poor agreement for smoke (only 13%) or fine absorbing aerosols (only 37%) relative to the other aerosol subtypes. Furthermore, polluted dust was found to be overused as an aerosol type by the CALIOP aerosol classification algorithm due to an attenuation-related depolarization bias [Burton *et al.*, 2013] in regions of heavy smoke.

To examine the extent of aerosol type misclassification by CALIOP specific to our domain, we compared the CALIOP-retrieved aerosol extinctions at 1064 nm for two cases: (i) extinction measurements with only the smoke aerosol flag and (ii) extinction measurements with both smoke and polluted dust aerosol flags. The results are shown for subregions B and C (Figure 10), where the majority of BB occurs. For subregion B (Figure 10a), the intense burning sources around 20°E (as discussed earlier) are now apparent in CALIOP extinction contours for combined smoke and polluted dust case. For subregion C, however, low surface elevations near the coast cause the lidar signal to get completely attenuated before reaching the bottom of the optically thick smoke plumes. Thus, high extinction values around 15°E (Figure 10b) end abruptly a few hundred meters above the ground even after considering smoke and polluted dust together. Over the ocean for both subregions B and C, the thickness of the aerosol above cloud layer is enhanced toward the bottom of the aerosol layers when smoke and polluted dust extinctions are combined as opposed to only smoke. This again appears to be a consequence of signal attenuation because even though southern Africa has a large area of arid terrain, dust from these sources do not get readily mobilized by the typical meteorology of the area [Liu *et al.*, 2015; Washington *et al.*, 2003]. However, it is interesting to note that

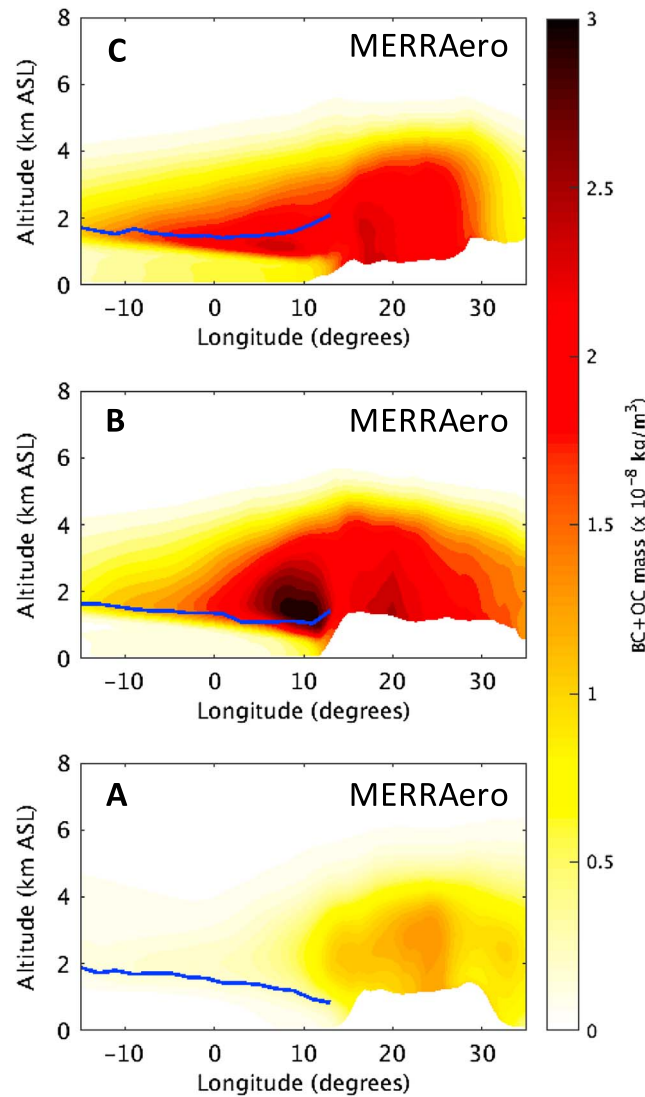


Figure 11. Meridional mean MERRAero smoke (BC + OC) aerosol mass concentrations ($\times 10^{-8} \text{ kg m}^{-3}$) averaged over August–September 2008 for the three subregions of the domain. CALIOP-retrieved mean cloud top heights are superimposed in blue over the ocean.

the highest extinction values over the ocean in CALIOP still occur at levels between 3 and 4 km irrespective of the inclusion or exclusion of polluted dust type with smoke.

5. Probable Causes of Differences in GEOS-5 and CALIOP Smoke Transport

It is clear from the previous discussions that the major differences between GEOS-5 and CALIOP smoke aerosol vertical distribution during the long-range transport of smoke plumes occur over the oceanic parts of the domain. To assess the persistence of this model behavior in the aerosol reanalysis product of GEOS-5: MERRAero [Buchard et al., 2015], specific to the time-period and domain of our study, we obtained the data for BB aerosol mass concentrations available at <https://gmao.gsfc.nasa.gov/reanalysis/merra/MERRAero/data/>. We found that the tendency of GEOS-5 smoke aerosol to rapidly descend toward the cloud tops off the coast and up to $\sim 0^\circ\text{W}$ persists in the MERRAero simulations as well (Figure 11). This indicates that assimilation of observed column AOD into the model is unable to resolve the inconsistencies between GEOS-5 and CALIOP observed aerosol vertical structure in this context. Out of the several aerosol-related processes listed in section 1 that could influence the vertical distribution of aerosol in a model, we may rule out the emission injection height treatment in GEOS-5 as a probable cause of observed differ-

ences because the simulated plume heights over land in all the models matched well with those from CALIOP. Similarly, inaccuracies in representation of emission source strength and physical aging of carbonaceous aerosol might alter the magnitudes of extinction profiles but cannot possibly explain the displacement of the peaks in the model extinction profiles to lower levels relative to CALIOP during the smoke plume transport over the ocean. Thus, investigations into the model representation of aerosol removal processes and convective transport are more relevant to the context of this study.

5.1. Aerosol Removal

Excessive removal of aerosol particles via gravitational settling or dry and wet depositions at levels of their predominant occurrence can cause a shift in the peak of extinction profiles during the transport of aerosol plumes. As discussed previously in section 2.1, CO can be a good tracer to test this hypothesis because CO and carbonaceous aerosol both have the same emission sources but unlike aerosol, CO does not get subjected to dry and wet depositions. In fact, Keil and Haywood [2003] observed the similarity in shape of the CO and aerosol vertical profiles retrieved from in situ measurements over the oceanic areas off the Namibian and Angolan coasts during the SAFARI 2000 campaign. Toward this end, we compare the

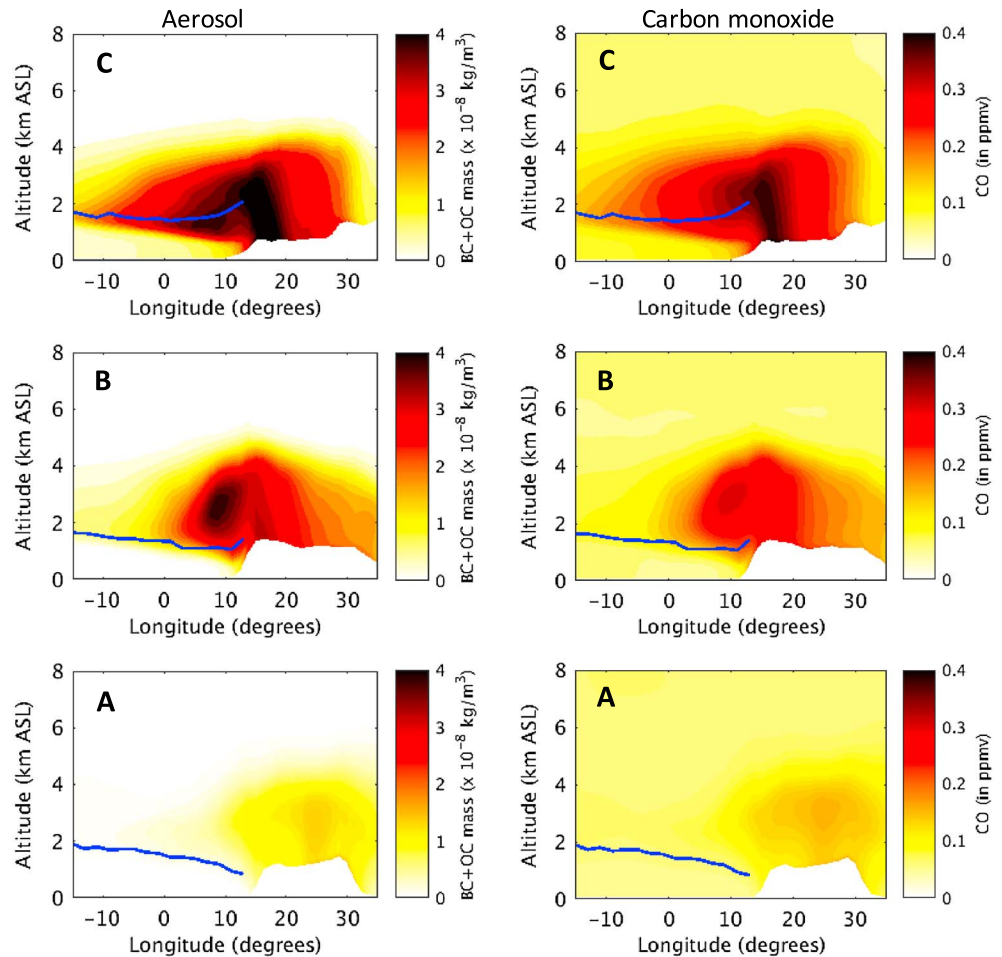


Figure 12. Contours of mean (left column) smoke aerosol mass concentrations ($\times 10^{-8} \text{ kg m}^{-3}$) and (right column) carbon monoxide (CO) mixing ratios (ppmv) simulated by GEOS-5-GOCART during August–September 2008 over the three subregions of the domain. CALIOP-retrieved cloud top heights are overlaid (in blue solid line) on all the subplots.

simulations of aerosol and CO transport from GEOS-5 using contours of smoke aerosol mass concentrations and CO mixing ratios, respectively (Figure 12). The BB emissions for both aerosol and CO here are based on the QFED2 inventory. There is profound similarity in the transport pattern of simulated smoke aerosol and CO plumes for most parts of the domain, suggesting a minimal role of aerosol removal processes in the observed discrepancies between the model and satellite measurements. The differences in the extents (both vertically and horizontally) to which CO gets transported compared to aerosols can be attributed to the longer lifetimes of CO (in the order of months) relative to the aerosols (approximately a week) [Bian *et al.*, 2013; Ford and Heald, 2012].

5.2. Convective Transport

Convection plays an important role in vertical transport and hence in the vertical distribution of aerosols and tracers in global models [Allen and Landuyt, 2014]. Convection occurs at a smaller spatial scale relative to the synoptic-scale processes and the typical resolution of global model grids [Belikov *et al.*, 2013]. Hence, shallow convection cannot be explicitly resolved but is instead parameterized in such models using different schemes or algorithms (Table 1). Discussions in section 4.3 suggested that the descending motion of smoke aerosols off the west coast was less rapid in CAM5 relative to GEOS-5 and other models in this study. Since the large-scale vertical motion seemed similar for both GEOS-5 and CAM5 over most parts of the domain except subregion C (Figure 9), we compared the amounts and locations of the upward convective motion within the models by considering the convective mass fluxes (CMFs) simulated by the two models (Figure 13). The GEOS-5-simulated CMFs over the ocean are up to about an order of magnitude lower

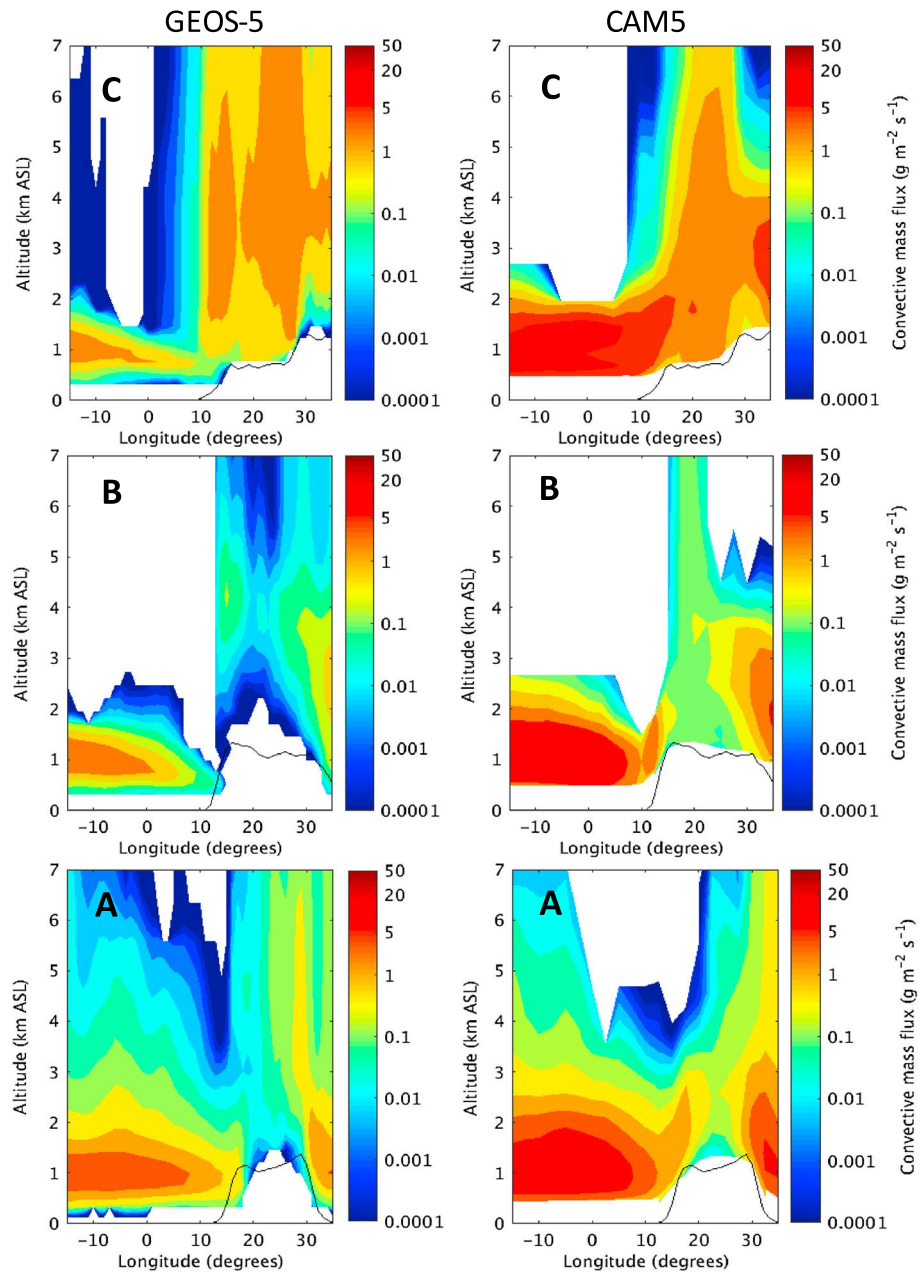


Figure 13. Comparison of convective mass flux (CMF, $\text{g m}^{-2} \text{s}^{-1}$) simulations by (left column) GEOS-5 and (right column) CAM5 during August–September 2008 over the three subregions of the domain. Note that the values are plotted on a log colorscale to account for the large difference in magnitudes of the simulated fluxes between the two models.

than CAM5-simulated CMFs. Further, strong CMFs over the ocean in CAM5 simulations extend up to the areas adjacent to the coast (5–10°E), while in GEOS-5, the strength of CMFs gradually diminish eastward and are almost negligible beyond 5°E, especially for subregions B and C. The vertical extent of CMFs is also higher for CAM5 compared to GEOS-5. These contrasts in magnitudes and distribution of CMFs cause the difference in intensity of convective lofting of aerosol plumes and hence correspond to the differences in vertical location of the smoke aerosol layer between CAM5 and GEOS-5 over the ocean. However, magnitudes of simulated shallow CMFs over the ocean are most pronounced only up to ~850–800 hPa (~1.5–2 km), inferring that convective lofting in the models cannot counter the strong subsidence experienced by the aerosol layers in the models above these levels.

5.3. Other Factors

Previous studies over the SE Atlantic, like *Sakaeda et al.* [2011], have found that substantial changes (~20–30%) in model-simulated large-scale vertical velocities can occur due to absorption of radiation at the levels of high BB aerosol loading, leading to a decrease in the model estimation of subsidence over the ocean. Similarly, *Colarco et al.* [2014] have found that stronger dust absorption in GEOS-5 can cause an increase in lofting of dust particles to higher altitudes during the transport of Saharan dust over the North Atlantic in the summer season. These examples indicate that inaccurate representation of aerosol absorption, which is very sensitive to the assumed single-scattering albedo, can also impact the simulation of large-scale vertical velocities and hence the vertical transport of aerosol in the model, owing to the aerosol-radiation feedback on the model atmosphere. The aerosol refractive index (at 550 nm) assumptions for models in Table 1 show that BC in CAM5 and ECHAM6 is very strongly absorbing relative to BC in other models. However, it is beyond the scope of our study to relate these differences in aerosol absorption amongst the models to the vertical transport of aerosol in the region. Thus, sensitivity studies to quantify the impact of aerosol absorption assumptions on the model-simulated vertical velocities over the SE Atlantic are suggested.

6. Conclusions

In this study, we evaluated the simulations of long-range transport and vertical distribution of BB aerosol by GEOS-5 and four other AeroCom models over the complete South African-Atlantic region using satellite observations for the peak BB months of August and September. The observations were derived from CALIOP version 3.01 Level 2 nighttime data for smoke extinctions at 1064 nm, which were converted to 550 nm for fair comparisons with the models using an appropriate value of the Ångström exponent for the region. The domain of interest was divided into three subregions to understand the distinct patterns of aerosol transport or vertical distribution that existed within the domain. Multimodel evaluation highlighted the discrepancies between the observed and simulated aerosol transport that might be common to most of the global models in this important region of BB. Possible causes of these discrepancies in the context of GEOS-5 were investigated to get directions toward improvement of the model performance in the region. The major findings of the study are summarized below.

1. The mean smoke AOD from our CALIOP gridded product was within 10–20% of mean MODIS AOD over both the land and oceanic parts of the domain. The magnitudes of BB AOD from GEOS-5 (with QFED2 emissions) were in good agreement with those from CALIOP over land areas, but the AOD gradient from land to ocean in GEOS-5 (~10% decrease) was found to be much lower than in CALIOP (~50% decrease). Using different BB emission inventories (QFED2 and GFED3), the GEOS-5 AOD could be changed by about a factor of 2. However, the horizontal and vertical distributions of BB aerosol in the model, including the AOD gradient from land to ocean are unaffected by the use of either of the emission inventories.
2. GEOS-5-simulated BB aerosol extinction profiles were consistent with CALIOP observations over the burning source region (over land). However, for areas downwind of the burning sources (over ocean), the peak of the model-simulated mean smoke extinction profiles occurs at altitudes 1–2 km lower than the peak of CALIOP-retrieved extinction profiles. In addition, GEOS-5-simulated clouds over the ocean appear to be more southward and farther away from the coast compared to MODIS clouds, with maximum cloud fraction values of only ~0.5 compared to 0.9 or higher from MODIS. Both these findings are crucial for studies quantifying the impact of absorbing aerosol on the underlying clouds in this region. The aerosol semidirect effect can change signs depending on whether the bulk of the absorbing aerosol occurs above or within cloud levels. Moreover, for the aerosol effects on clouds to effectively feed back to the model climate, aerosol-cloud overlap and cloud amounts need to be accurately simulated.
3. Multimodel evaluation of BB aerosol plume transport using CALIOP observations showed that models were, in general, able to capture the aerosol plume top heights over land, irrespective of the differences in emission injection height assumptions. Over the ocean, however, the modeled aerosol plumes quickly descend to lower levels just off the west coast, relative to the heights up to which they were lofted over land. In contrast, CALIOP smoke plumes continue their horizontal transport at elevated levels above the MBL (with extinction peaks between 3 and 4 km asl). The levels to which the aerosol plumes get subsided and the steepness of their descent vary amongst the models and also amongst the different subregions in the domain. Overall, CAM5-simulated BB aerosol transport over the ocean showed closer agreement with CALIOP observations compared to the other models in this study.

Acknowledgments

This study was supported by NASA grant NNX10AG61G to Purdue University. We thank Benjamin Johnson (UK Met Office) and Mariya Petrenko (NASA GSFC) for their input during the analysis of AeroCom BB experiment results. We thank the AeroCom Team for providing us access to their data server. We would also like to acknowledge NASA Earth Science Division for their support. K. Zhang and H. Wang acknowledge support from the U.S. Department of Energy (DOE), Office of Science, Biological and Environmental Research as part of the Earth System Modeling Program. The Pacific Northwest National Laboratory (PNNL) is operated for DOE by Battelle Memorial Institute under contract DE-AC05-76RLO1830. X. Liu would like to acknowledge the support by the Office of Science of the U.S. Department of Energy (DOE) as the NSF-DOE-USDA Joint Earth System Modeling (EaSM) Program. K. Zhang, H. Wang, and X. Liu also acknowledge the use of computational resources (ark:/85065/d7wd3xhc) at the NCAR-Wyoming Supercomputing Center provided by the National Science Foundation and the State of Wyoming and supported by NCAR's Computational and Information Systems Laboratory. The work of T. Mielenon was funded by the Academy of Finland Centre of Excellence in Atmospheric Science (272041). G. Curci thanks the Euro Mediterranean Center for Climate Change (CMCC), Lecce, Italy, for providing computational resources. A. P. Protonotariou would like to acknowledge the Computer Center of National and Kapodistrian University of Athens and the Greek Research and Technology Network (GRNET) in the National HPC facility-ARIS for supporting part of this work by granting computational time. The Level 2 CALIOP data were obtained from the NASA Langley Research Center Atmospheric Science Data Center. The AeroCom data used to obtain the aerosol extinctions in this paper are available on the AeroCom Database and User Server (aerocom-users.met.no). They are accessible upon request, following the AeroCom Policy and access conditions described under <http://aerocom.met.no/data.html>. The GEOS-5 model outputs or any other data needed to reproduce the results described in this paper are archived at Purdue Research Computing (RCAC) provided High Performance Storage System. These are available upon request from the corresponding author (das22@purdue.edu). Finally, we thank the reviewers for their constructive and helpful comments that helped us improve the original manuscript.

- Investigations into the possible causes of differences in GEOS-5 and CALIOP smoke transport over the ocean indicated that aerosol removal processes in GEOS-5 play a minor role in causing the observed differences. Instead, there is most likely an overestimation of subsidence over the ocean in the model-simulated large-scale vertical velocities. Large differences in model-simulated offshore CMFs between GEOS-5 and CAM5 in terms of both intensity and spatial distribution suggest further investigations toward evaluation of GEOS-5-simulated convective transport in this region. At the same time, possible discrepancies in model CMFs cannot solely explain the differences in GEOS-5 and CALIOP smoke transport at altitudes above 2 km over the ocean.

References

- Abel, S. J., E. J. Highwood, J. M. Haywood, and M. A. Stringer (2005), The direct radiative effect of biomass burning aerosols over southern Africa, *Atmos. Chem. Phys.*, *5*(7), 1999–2018, doi:10.5194/acp-5-1999-2005.
- Adebiyi, A. A., P. Zuidema, and S. J. Abel (2015), The convolution of dynamics and moisture with the presence of shortwave absorbing aerosols over the Southeast Atlantic, *J. Clim.*, *28*(5), 1997–2024, doi:10.1175/JCLI-D-14-00352.1.
- Allen, R. J., and W. Landuyt (2014), The vertical distribution of black carbon in CMIP5 models: Comparison to observations and the importance of convective transport, *J. Geophys. Res. Atmos.*, *119*, 4808–4835, doi:10.1002/2014JD021595.
- Anderson, B. E., W. B. Grant, G. L. Gregory, E. V. Browell, J. E. Collins, G. W. Sachse, D. R. Bagwell, C. H. Hudgins, D. R. Blake, and N. J. Blake (1996), Aerosols from biomass burning over the tropical South Atlantic region: Distributions and impacts, *J. Geophys. Res.*, *101*(D19), 24117–24137, doi:10.1029/96JD00717.
- Andreae, M. O., and P. Merlet (2001), Emission of trace gases and aerosols from biomass burning, *Global Biogeochem. Cycles*, *15*(4), 955–966, doi:10.1029/2000GB001382.
- Belikov, D. A., et al. (2013), Off-line algorithm for calculation of vertical tracer transport in the troposphere due to deep convection, *Atmos. Chem. Phys.*, *13*(3), 1093–1114, doi:10.5194/acp-13-1093-2013.
- Bey, I., D. J. Jacob, R. M. Yantosca, J. A. Logan, B. D. Field, A. M. Fiore, Q. Li, H. Y. Liu, L. J. Mickley, and M. G. Schultz (2001), Global modeling of tropospheric chemistry with assimilated meteorology: Model description and evaluation, *J. Geophys. Res.*, *106*(D19), 23,073–23,095, doi:10.1029/2001JD000807.
- Bian, H., M. Chin, S. R. Kawa, B. Duncan, A. Arellano, and P. Kasibhatla (2007), Sensitivity of global CO simulations to uncertainties in biomass burning sources, *J. Geophys. Res.*, *112*, D23308, doi:10.1029/2006JD008376.
- Bian, H., M. Chin, S. R. Kawa, H. Yu, T. Diehl, and T. Kucsera (2010), Multiscale carbon monoxide and aerosol correlations from satellite measurements and the GOCART model: Implication for emissions and atmospheric evolution, *J. Geophys. Res.*, *115*, D07302, doi:10.1029/2009JD012781.
- Bian, H., et al. (2013), Source attributions of pollution to the Western Arctic during the NASA ARCTAS field campaign, *Atmos. Chem. Phys.*, *13*(9), 4707–4721, doi:10.5194/acp-13-4707-2013.
- Bond, T. C., et al. (2013), Bounding the role of black carbon in the climate system: A scientific assessment, *J. Geophys. Res. Atmos.*, *118*, 5380–5552, doi:10.1002/jgrd.50171.
- Buchard, V., A. M. da Silva, P. R. Colarco, A. Darnenov, C. A. Randles, R. Govindaraju, O. Torres, J. Campbell, and R. Spurr (2015), Using the OMI aerosol index and absorption aerosol optical depth to evaluate the NASA MERRA Aerosol Reanalysis, *Atmos. Chem. Phys.*, *15*(10), 5743–5760, doi:10.5194/acp-15-5743-2015.
- Burton, S. P., R. A. Ferrare, M. A. Vaughan, A. H. Omar, R. R. Rogers, C. A. Hostetler, and J. W. Hair (2013), Aerosol classification from airborne HSRL and comparisons with the CALIPSO vertical feature mask, *Atmos. Meas. Tech.*, *6*(5), 1397–1412, doi:10.5194/amt-6-1397-2013.
- Chand, D., R. Wood, T. L. Anderson, S. K. Satheesh, and R. J. Charlson (2009), Satellite-derived direct radiative effect of aerosols dependent on cloud cover, *Nat. Geosci.*, *2*(3), 181–184, doi:10.1038/Ngeo437.
- Chin, M., P. Ginoux, S. Kinne, O. Torres, B. N. Holben, B. N. Duncan, R. V. Martin, J. A. Logan, A. Higurashi, and T. Nakajima (2002), Tropospheric aerosol optical thickness from the GOCART model and comparisons with satellite and Sun photometer measurements, *J. Atmos. Sci.*, *59*(3), 461–483, doi:10.1175/1520-0469(2002)059<0461:Taotft>2.0.Co;2.
- Chin, M., A. Chu, R. Levy, L. Remer, Y. Kaufman, B. Holben, T. Eck, P. Ginoux, and Q. Gao (2004), Aerosol distribution in the Northern Hemisphere during ACE-Asia: Results from global model, satellite observations, and Sun photometer measurements, *J. Geophys. Res.*, *109*, D23S90, doi:10.1029/2004JD004829.
- Chin, M., T. Diehl, O. Dubovik, T. F. Eck, B. N. Holben, A. Sinyuk, and D. G. Streets (2009), Light absorption by pollution, dust, and biomass burning aerosols: A global model study and evaluation with AERONET measurements, *Ann. Geophys.*, *27*(9), 3439–3464, doi:10.5194/angeo-27-3439-2009.
- Colarco, P., A. da Silva, M. Chin, and T. Diehl (2010), Online simulations of global aerosol distributions in the NASA GEOS-4 model and comparisons to satellite and ground-based aerosol optical depth, *J. Geophys. Res.*, *115*, D14207, doi:10.1029/2009JD012820.
- Colarco, P., E. P. Nowottnick, C. A. Randles, B. Yi, P. Yang, K.-M. Kim, J. A. Smith, and C. G. Bardeen (2014), Impact of radiatively interactive dust aerosols in the NASA GEOS-5 climate model: Sensitivity to dust particle shape and refractive index, *J. Geophys. Res. Atmos.*, *119*, 753–786, doi:10.1002/2013JD020046.
- Cooke, W. F., C. Lioussé, H. Cachier, and J. Feichter (1999), Construction of a $1^\circ \times 1^\circ$ fossil fuel emission data set for carbonaceous aerosol and implementation and radiative impact in the ECHAM4 model, *J. Geophys. Res.*, *104*(D18), 22,137–22,162, doi:10.1029/1999JD900187.
- Costantino, L., and F. M. Bréon (2010), Analysis of aerosol-cloud interaction from multi-sensor satellite observations, *Geophys. Res. Lett.*, *37*, L11801, doi:10.1029/2009GL041828.
- Costantino, L., and F. M. Bréon (2013), Aerosol indirect effect on warm clouds over South-East Atlantic, from co-located MODIS and CALIPSO observations, *Atmos. Chem. Phys.*, *13*(1), 69–88, doi:10.5194/acp-13-69-2013.
- Curci, G., et al. (2014), Uncertainties of simulated aerosol optical properties induced by assumptions on aerosol physical and chemical properties: An AQMEII-2 perspective, *Atmos. Environ.*, *115*, 541–552, doi:10.1016/j.atmosenv.2014.09.009.
- Darnenov, A., and A. da Silva (2015), The Quick Fire Emissions Dataset (QFED): Documentation of versions 2.1, 2.2 and 2.4, *NASA/TM-2015-104606*, vol. 38.
- Denstener, F., et al. (2006), Emissions of primary aerosol and precursor gases in the years 2000 and 1750 prescribed data-sets for AeroCom, *Atmos. Chem. Phys.*, *6*, 4321–4344, doi:10.5194/acp-6-4321-2006.

- Derbyshire, S. H., A. V. Maidens, S. F. Milton, R. A. Stratton, and M. R. Willett (2011), Adaptive detrainment in a convective parametrization, *Q. J. Roy. Meteorol. Soc.*, *137*(660), 1856–1871, doi:10.1002/qj.875.
- Eck, T. F., et al. (2013), A seasonal trend of single scattering albedo in southern African biomass-burning particles: Implications for satellite products and estimates of emissions for the world's largest biomass-burning source, *J. Geophys. Res. Atmos.*, *118*, 6414–6432, doi:10.1002/jgrd.50500.
- Edwards, D. P., et al. (2006), Satellite-observed pollution from Southern Hemisphere biomass burning, *J. Geophys. Res.*, *111*, D14312, doi:10.1029/2005JD006655.
- Ford, B., and C. L. Heald (2012), An A-train and model perspective on the vertical distribution of aerosols and CO in the Northern Hemisphere, *J. Geophys. Res.*, *117*, D06211, doi:10.1029/2011JD016977.
- Gregory, D., and P. R. Rowntree (1990), A mass flux convection scheme with representation of cloud ensemble characteristics and stability-dependent closure, *Mon. Weather Rev.*, *118*(7), 1483–1506, doi:10.1175/1520-0493(1990)118<1483:AMFCSW>2.0.CO;2.
- Hao, W. M., D. E. Ward, G. Olbu, and S. P. Baker (1996), Emissions of CO₂, CO, and hydrocarbons from fires in diverse African savanna ecosystems, *J. Geophys. Res.*, *101*(D19), 23,577–23,584, doi:10.1029/95JD02198.
- Haywood, J. M., S. R. Osborne, and S. J. Abel (2004), The effect of overlying absorbing aerosol layers on remote sensing retrievals of cloud effective radius and cloud optical depth, *Q. J. R. Meteorol. Soc.*, *130*(598), 779–800, doi:10.1256/qj.03.100.
- Hess, M., P. Koepke, and I. Schult (1998), Optical Properties of Aerosols and Clouds: The software package OPAC, *Bull. Am. Meteorol. Soc.*, *79*(5), 831–844, doi:10.1175/1520-0477(1998)079<0831:OPOAAC>2.0.CO;2.
- Hunt, W. H., D. M. Winker, M. A. Vaughan, K. A. Powell, P. L. Lucker, and C. Weimer (2009), CALIPSO lidar description and performance assessment, *J. Atmos. Oceanic Tech.*, *26*(7), 1214–1228, doi:10.1175/2009JTECHA1223.1.
- Jethva, H., O. Torres, F. Waquet, D. Chand, and Y. Hu (2014), How do A-train sensors intercompare in the retrieval of above-cloud aerosol optical depth? A case study-based assessment, *Geophys. Res. Lett.*, *41*, 186–192, doi:10.1002/2013GL058405.
- Johnson, B. T., K. P. Shine, and P. M. Forster (2004), The semi-direct aerosol effect: Impact of absorbing aerosols on marine stratocumulus, *Q. J. R. Meteorol. Soc.*, *130*(599), 1407–1422, doi:10.1256/qj.03.61.
- Johnson, B. T., et al. (2016), Evaluation of biomass burning aerosols in the HadGEM3 climate model with observations from the SAMBBA field campaign, *Atmos. Chem. Phys. Discuss.*, *16*, 14,657–14,685, doi:10.5194/acp-2016-442.
- Kacenenbogen, M., J. Redemann, M. A. Vaughan, A. H. Omar, P. B. Russell, S. Burton, R. R. Rogers, R. A. Ferrare, and C. A. Hostetler (2014), An evaluation of CALIOP/CALIPSO's aerosol-above-cloud detection and retrieval capability over North America, *J. Geophys. Res. Atmos.*, *119*, 230–244, doi:10.1002/2013JD020178.
- Kaufman, Y. J., J. M. Haywood, P. V. Hobbs, W. Hart, R. Kleidman, and B. Schmid (2003), Remote sensing of vertical distributions of smoke aerosol off the coast of Africa, *Geophys. Res. Lett.*, *30*(16), 1831, doi:10.1029/2003GL017068.
- Keil, A., and J. M. Haywood (2003), Solar radiative forcing by biomass burning aerosol particles during SAFARI 2000: A case study based on measured aerosol and cloud properties, *J. Geophys. Res.*, *108*(D13), 8467, doi:10.1029/2002JD002315.
- Kinne, S., et al. (2006), An AeroCom initial assessment—Optical properties in aerosol component modules of global models, *Atmos. Chem. Phys.*, *6*(7), 1815–1834, doi:10.5194/acp-6-1815-2006.
- Koch, D., and A. D. Del Genio (2010), Black carbon semi-direct effects on cloud cover: Review and synthesis, *Atmos. Chem. Phys.*, *10*(16), 7685–7696, doi:10.5194/acp-10-7685-2010.
- Koffi, B., et al. (2012), Application of the CALIOP layer product to evaluate the vertical distribution of aerosols estimated by global models: AeroCom phase I results, *J. Geophys. Res.*, *117*, D10201, doi:10.1029/2011JD016858.
- Koffi, B., et al. (2016), Evaluation of the aerosol vertical distribution in global aerosol models through comparison against CALIOP measurements: AeroCom phase II results, *J. Geophys. Res. Atmos.*, *121*, 7254–7283, doi:10.1002/2015JD024639.
- Levy, R. C., L. A. Remer, R. G. Kleidman, S. Mattoo, C. Ichoku, R. Kahn, and T. F. Eck (2010), Global evaluation of the Collection 5 MODIS dark-target aerosol products over land, *Atmos. Chem. Phys.*, *10*, 10,399–10,420, doi:10.5194/acp-10-10399-2010.
- Liu, X., et al. (2012), Toward a minimal representation of aerosols in climate models: Description and evaluation in the Community Atmosphere Model CAM5, *Geosci. Model Dev.*, *5*(3), 709–739, doi:10.5194/gmd-5-709-2012.
- Liu, Z. Y., M. Vaughan, D. Winker, C. Kittaka, B. Getzewich, R. Kuehn, A. Omar, K. Powell, C. Trepte, and C. Hostetler (2009), The CALIPSO lidar cloud and aerosol discrimination: Version 2 algorithm and initial assessment of performance, *J. Atmos. Oceanic Tech.*, *26*(7), 1198–1213, doi:10.1175/2009jtecha1229.1.
- Liu, Z. Y., D. Winker, A. Omar, M. Vaughan, J. Kar, C. Trepte, Y. Hu, and G. Schuster (2015), Evaluation of CALIOP 532 nm aerosol optical depth over opaque water clouds, *Atmos. Chem. Phys.*, *15*(3), 1265–1288, doi:10.5194/acp-15-1265-2015.
- Maria, S. F., L. M. Russell, M. K. Gilles, and S. C. B. Myneni (2004), Organic aerosol growth mechanisms and their climate-forcing implications, *Science*, *306*(5703), 1921–1924, doi:10.1126/science.1103491.
- McFarquhar, G. M., and H. Wang (2006), Effects of aerosols on trade wind cumuli over the Indian Ocean: Model simulations, *Q. J. Roy. Meteorol. Soc.*, *132*(616), 821–843, doi:10.1256/qj.04.179.
- Mechoso, C. R., et al. (2013), Ocean–cloud–atmosphere–land interactions in the southeastern Pacific: The VOCALS program, *B. Am. Meteorol. Soc.*, *95*(3), 357–375, doi:10.1175/BAMS-D-11-00246.1.
- Meyer, K., S. Platnick, L. Oreopoulos, and D. Lee (2013), Estimating the direct radiative effect of absorbing aerosols overlying marine boundary layer clouds in the southeast Atlantic using MODIS and CALIOP, *J. Geophys. Res. Atmos.*, *118*, 4801–4815, doi:10.1002/jgrd.50449.
- Mielonen, T., A. Arola, M. Komppula, J. Kukkonen, J. Koskinen, G. de Leeuw, and K. E. J. Lehtinen (2009), Comparison of CALIOP level 2 aerosol subtypes to aerosol types derived from AERONET inversion data, *Geophys. Res. Lett.*, *36*, L18804, doi:10.1029/2009GL039609.
- Moorthi, S., and M. J. Suarez (1992), Relaxed Arakawa-Schubert. A parameterization of moist convection for general circulation models, *Mon. Weather Rev.*, *120*(6), 978–1002, doi:10.1175/1520-0493(1992)120<0978:RASAP0>2.0.CO;2.
- Myhre, G., et al. (2013), Radiative forcing of the direct aerosol effect from AeroCom Phase II simulations, *Atmos. Chem. Phys.*, *13*(4), 1853–1877, doi:10.5194/acp-13-1853-2013.
- Nordeng, T. E. (1994), Extended versions of the convective parametrization scheme at ECMWF and their impact on the mean and transient activity of the model in the tropics, *Tech. Memo.*, *206*, ECMWF.
- Omar, A. H., et al. (2009), The CALIPSO automated aerosol classification and lidar ratio selection algorithm, *J. Atmos. Oceanic Tech.*, *26*(10), 1994–2014, doi:10.1175/2009JTECHA1231.1.
- Painemal, D., S. Kato, and P. Minnis (2014), Boundary layer regulation in the southeast Atlantic cloud microphysics during the biomass burning season as seen by the A-train satellite constellation, *J. Geophys. Res. Atmos.*, *119*, 11,288–11,302, doi:10.1002/2014JD022182.
- Park, S., and C. S. Bretherton (2009), The University of Washington shallow convection and moist turbulence schemes and their impact on climate simulations with the Community Atmosphere Model, *J. Clim.*, *22*(12), 3449–3469, doi:10.1175/2008JCLI2557.1.

- Penner, J. E., S. Y. Zhang, and C. C. Chuang (2003), Soot and smoke aerosol may not warm climate, *J. Geophys. Res.*, *108*(D21), 4657, doi:10.1029/2003JD003409.
- Protonotariou, A. P., M. Tombrou, C. Giannakopoulos, E. Kostopoulou, and P. Le Sager (2010), Study of CO surface pollution in Europe based on observations and nested-grid applications of GEOS-CHEM global chemical transport model, *Tellus B*, *62*, 209–227, doi:10.1111/j.1600-0889.2010.00462.x.
- Ramanathan, V., P. J. Crutzen, J. T. Kiehl, and D. Rosenfeld (2001), Aerosols, climate, and the hydrological cycle, *Science*, *294*(5549), 2119–2124, doi:10.1126/science.1064034.
- Randerson, J. T., G. R. van der Werf, L. Giglio, G. J. Collatz, and P. Kasibhatla (2013), Global Fire Emissions Database, version 3 (GFEDv3.1). Available on-line from Oak Ridge National Laboratory Distributed Active Archive Center, Oak Ridge, Ten., USA, doi:10.3334/ORNLDAA/1191.
- Randles, C. A., P. R. Colarco, and A. da Silva (2013), Direct and semi-direct aerosol effects in the NASA GEOS-5 AGCM: Aerosol-climate interactions due to prognostic versus prescribed aerosols, *J. Geophys. Res. Atmos.*, *118*, 149–169, doi:10.1029/2012JD018388.
- Randles, C. A., and V. Ramaswamy (2010), Direct and semi-direct impacts of absorbing biomass burning aerosol on the climate of southern Africa: A Geophysical Fluid Dynamics Laboratory GCM sensitivity study, *Atmos. Chem. Phys.*, *10*(20), 9819–9831, doi:10.5194/acp-10-9819-2010.
- Rienecker, M. M., et al. (2011), MERRA: NASA's Modern-Era Retrospective Analysis for Research and Applications, *J. Clim.*, *24*(14), 3624–3648, doi:10.1175/JCLI-D-11-00015.1.
- Rienecker, M. M., et al. (2008), The GEOS-5 data assimilation system—Documentation of version 5.0.1, 5.1.0, and 5.2.0, *NASA TM/2008-104606*, vol. 27, 118 pp.
- Roekner, E., R. Brokopf, M. Esch, M. Giorgetta, S. Hagemann, L. Kornbluh, E. Manzini, U. Schlese, and U. Schulzweida (2006), Sensitivity of simulated climate to horizontal and vertical resolution in the ECHAM5 atmosphere model, *J. Clim.*, *19*(16), 3771–3791, doi:10.1175/JCLI3824.1.
- Sakaeda, N., R. Wood, and P. J. Rasch (2011), Direct and semidirect aerosol effects of southern African biomass burning aerosol, *J. Geophys. Res.*, *116*, D12205, doi:10.1029/2010JD015540.
- Samset, B. H., et al. (2013), Black carbon vertical profiles strongly affect its radiative forcing uncertainty, *Atmos. Chem. Phys.*, *13*(5), 2423–2434, doi:10.5194/acp-13-2423-2013.
- Schulz, M., et al. (2006), Radiative forcing by aerosols as derived from the AeroCom present-day and pre-industrial simulations, *Atmos. Chem. Phys.*, *6*(12), 5225–5246, doi:10.5194/acp-6-5225-2006.
- Stevens, B., et al. (2013), Atmospheric component of the MPI-M Earth System Model: ECHAM6, *J. Adv. Model Earth Sy.*, *5*(2), 146–172, doi:10.1002/jame.20015.
- Stier, P., et al. (2013), Host model uncertainties in aerosol radiative forcing estimates: Results from the AeroCom prescribed intercomparison study, *Atmos. Chem. Phys.*, *13*(6), 3245–3270, doi:10.5194/acp-13-3245-2013.
- Streets, D. G., F. Yan, M. Chin, T. Diehl, N. Mahowald, M. Schultz, M. Wild, Y. Wu, and C. Yu (2009), Anthropogenic and natural contributions to regional trends in aerosol optical depth, 1980–2006, *J. Geophys. Res.*, *114*, D00D18, doi:10.1029/2008JD011624.
- Textor, C., et al. (2006), Analysis and quantification of the diversities of aerosol life cycles within AeroCom, *Atmos. Chem. Phys.*, *6*(7), 1777–1813, doi:10.5194/acp-6-1777-2006.
- Tiedtke, M. (1989), A comprehensive mass flux scheme for cumulus parameterization in large-scale models, *Mon. Weather Rev.*, *117*(8), 1779–1800, doi:10.1175/1520-0493(1989)117<1779:ACMFSF>2.0.CO;2.
- Torres, O., C. Ahn, and Z. Chen (2013), Improvements to the OMI near-UV aerosol algorithm using A-train CALIOP and AIRS observations, *Atmos. Meas. Tech.*, *6*, 3257–3270, doi:10.5194/amt-6-3257-2013.
- van der Werf, G. R., J. T. Randerson, L. Giglio, G. J. Collatz, P. S. Kasibhatla, and A. F. Arellano Jr. (2006), Interannual variability in global biomass burning emissions from 1997 to 2004, *Atmos. Chem. Phys.*, *6*(11), 3423–3441, doi:10.5194/acp-6-3423-2006.
- van der Werf, G. R., J. T. Randerson, L. Giglio, G. J. Collatz, M. Mu, P. S. Kasibhatla, D. C. Morton, R. S. DeFries, Y. Jin, and T. T. van Leeuwen (2010), Global fire emissions and the contribution of deforestation, savanna, forest, agricultural, and peat fires (1997–2009), *Atmos. Chem. Phys.*, *10*(23), 11707–11735, doi:10.5194/acp-10-11707-2010.
- Vaughan, M. A., et al. (2009), Fully automated detection of cloud and aerosol layers in the CALIPSO lidar measurements, *J. Atmos. Oceanic Tech.*, *26*(10), 2034–2050, doi:10.1175/2009JTECHA1228.1.
- Washington, R., M. Todd, N. J. Middleton, and A. S. Goudie (2003), Dust-storm source areas determined by the Total Ozone Monitoring Spectrometer and surface observations, *Ann. Assoc. Am. Geogr.*, *93*(2), 297–313, doi:10.1111/1467-8306.9302003.
- Wilcox, E. M. (2010), Stratocumulus cloud thickening beneath layers of absorbing smoke aerosol, *Atmos. Chem. Phys.*, *10*(23), 11769–11777, doi:10.5194/acp-10-11769-2010.
- Wilcox, E. M. (2012), Direct and semi-direct radiative forcing of smoke aerosols over clouds, *Atmos. Chem. Phys.*, *12*(1), 139–149, doi:10.5194/acp-12-139-2012.
- Winker, D. M., J. L. Tackett, B. J. Getzewich, Z. Liu, M. A. Vaughan, and R. R. Rogers (2013), The global 3-D distribution of tropospheric aerosols as characterized by CALIOP, *Atmos. Chem. Phys.*, *13*(6), 3345–3361, doi:10.5194/acp-13-3345-2013.
- Winker, D. M., M. A. Vaughan, A. Omar, Y. X. Hu, K. A. Powell, Z. Y. Liu, W. H. Hunt, and S. A. Young (2009), Overview of the CALIPSO mission and CALIOP data processing algorithms, *J. Atmos. Oceanic Tech.*, *26*(11), 2310–2323, doi:10.1175/2009jtech1281.1.
- Young, S. A., and M. A. Vaughan (2009), The retrieval of profiles of particulate extinction from Cloud-Aerosol Lidar Infrared Pathfinder Satellite Observations (CALIPSO) data: Algorithm description, *J. Atmos. Oceanic Tech.*, *26*(6), 1105–1119, doi:10.1175/2008JTECHA1221.1.
- Yu, H., M. Chin, D. M. Winker, A. H. Omar, Z. Liu, C. Kittaka, and T. Diehl (2010), Global view of aerosol vertical distributions from CALIPSO lidar measurements and GOCART simulations: Regional and seasonal variations, *J. Geophys. Res.*, *115*, D00H30, doi:10.1029/2009JD013364.
- Zhang, G. J., and N. A. McFarlane (1995), Sensitivity of climate simulations to the parameterization of cumulus convection in the Canadian climate Centre general circulation model, *Atmos. Ocean*, *33*(3), 407–446, doi:10.1080/07055900.1995.9649539.